Global transverse energy distributions in relativistic nuclear collisions at 14.6A GeV/c

T. Abbott,[4],[a] Y. Akiba,[7] D. Alburger,[2] D. Beavis,[2] L. Birstein,[2] M.A. Bloomer,[9],[b] P.D. Bond,[2] C. Chasman,[2] Z. Chen,[2] Y.Y. Chu,[2] B.A. Cole,[9],[c] J.B. Costales,[9],[d] H.J. Crawford,[3] J.B. Cumming,[2] R. Debbe,[2] E. Duek,[2],[e] J. Engelage,[3] S.Y. Fung,[4] L. Grodzins,[9] S. Gushue,[2] H. Hamagaki,[7] O. Hansen,[2] R.S. Hayano,[10] S. Hayashi,[7],[f] S. Homma,[7] H.Z. Huang,[9],[b] Y. Ikeda,[8],[g] I. Juricic,[5],[h] J. Kang,[4] S. Katcoff,[2] S. Kaufman,[1] K. Kimura,[8] K. Kitamura,[6],[i] K. Kurita,[5],[j] R.J. Ledoux,[9] M.J. LeVine,[2] Y. Miake,[2] R.J. Morse,[9],[b] B. Moskowitz,[2] S. Nagamiya,[5] J. Olness,[2] C.G. Parsons,[9] L.P. Remsberg,[2] H. Sakurai,[10] M. Sarabura,[9],[k] A. Shor,[2],[l] P. Stankus,[5] S.G. Steadman,[9] G.S.F. Stephans,[9] T. Sugitate,[6] M. Tanaka,[2] M.J. Tannenbaum,[2] M. Torikoshi,[7],[m] J.H. van Dijk,[2] F. Videbæk,[1],[f] M. Vient,[4],[n] P. Vincent,[2],[o] E. Vulgaris,[9],[p] V. Vutsadakis,[9] W.A. Watson III,[2],[q] H.E. Wegner,[2] D.S. Woodruff,[9] Y.D. Wu,[5] and W. Zajc[5]

(E-802 Collaboration)

[1] Argonne National Laboratory, Argonne, Illinois 60439
[2] Brookhaven National Laboratory, Upton, New York 11973
[3] Space Sciences Laboratory, University of California, Berkeley, California 94720
[4] University of California, Riverside, California 92507
[5] Columbia University, New York, New York 10027
and Nevis Laboratories, Irvington, New York 10533
[6] Hiroshima University, Hiroshima 730, Japan
[7] Institute for Nuclear Study, University of Tokyo, Tokyo 188, Japan
[8] Kyushu University, Fukuoka 812, Japan
[9] Massachusetts Institute of Technology, Cambridge, Massachusetts 02139
[10] Department of Physics, University of Tokyo, Tokyo 113, Japan
(Received 7 February 1992)

A systematic set of measurements of the global transverse energy distributions, $d\sigma/dE_T$ and $dE_T/d\eta$, from beams of protons, ^{16}O and ^{28}Si at 14.6A GeV/c, incident on targets ranging from Be to Au is presented. The detector was a semicircular array of lead-glass blocks, covering polar angles $9° < \theta < 32°$, whose total response provides a good measure of the produced particle yield in the central rapidity region of these reactions. Proton-nucleus spectra exhibit a similar shape on the high-energy tail, independent of target, suggesting that produced particles in such events arise mostly from the first collision of the projectile proton. For targets heavier than Cu, the high-energy edges of the oxygen-nucleus spectra, and of the silicon-nucleus spectra, reach ratios consistent with the geometry of central collisions. Angular distributions, $dE_T/d\eta$, are characterized by Gaussian fits, and an acceptance-independent form of the differential cross section is found, based on the maximum value of $dE_T/d\eta$. The projectile dependence of nucleus-nucleus spectra is studied in terms of two very different models: simple energy scaling and the wounded projectile nucleon model of $p+A$ convolutions.

PACS number(s): 25.75.+r

[a] Now at Xon Tech, Inc., Van Nuys, CA 91406.
[b] Now at Lawrence Berkeley Laboratory, Berkeley, CA 94720.
[c] Now at Nevis Laboratories, Irvington, NY 10533.
[d] Now at Lawrence Livermore National Laboratory, Livermore, CA 94550.
[e] Now at Superconducting Super Collider Laboratory, Dallas, TX 75237.
[f] Now at Brookhaven National Laboratory, Upton, NY 11973.
[g] Now at Hitachi Limited, Hitachi, Ibaraki 316, Japan.
[h] Now at Schlumberger Corp., Houston, TX 77210.
[i] Now at Nippon Telegraph and Telephone Co., Tsuyama, Okayama 708, Japan.
[j] Now at University of Tsukuba, Tsukuba, Ibaraki 305, Japan.
[k] Now at Los Alamos National Laboratory, Los Alamos, NM 87545.
[l] Now at Weizmann Institute of Science, Rehovot 76100, Israel.
[m] Now at Mitsubishi Electric Co., Hyogo 652, Japan.
[n] Now at UC Irvine, Irvine, CA 92717.
[o] Now at Bruker Medical Imaging, Inc., Lisle, IL 60532.
[p] Now at Bell Telephone Laboratory, Naperville, IL 60566.
[q] Now at CEBAF, Newport News, VA 23606.

I. INTRODUCTION

Relativistic heavy ion physics aims to probe previously experimentally inaccessible regions of high energy and baryon density of nuclear matter. Much of the motivation arises from the prediction of a new state in which the individual quarks are deconfined: the quark-gluon plasma. Global transverse energy (E_T) spectra of produced particles provide information concerning the nuclear collision dynamics. They are an indicator of the impact parameter (centrality) of collisions, and the magnitude of $dE_T/d\eta$ may be used to estimate the thermal energy density in a model-dependent manner [1]. Another important, related, issue is the degree of "stopping" of the incident projectile baryons.

The richness of experimental E_T data now available is attested to by earlier work done at the CERN ISR [2], the publications of several groups working both at the BNL AGS [3–5] and at the CERN SPS [6–9], as well as recent review articles on the subject [10]. In particular, the first measurements of $^{16}O+A$ at the AGS beam momentum of $14.6A$ GeV/c implied that the oxygen projectile can be "substantially stopped" by targets the size of copper or larger so that additional pion production effectively ceases [3].

The purpose of this paper is to present a systematic set of measured transverse energy spectra for the central rapidity region at the incident beam momentum of $14.6A$ GeV/c. The results presented here are for three different projectiles: protons from the Brookhaven Linac-AGS, and ^{16}O and ^{28}Si from the Brookhaven Tandem-AGS Complex. The targets used were Be, C, Al, Cu, Ag, and Au, as summarized in Table I. All spectra were measured in the identical detector, minimizing the role of systematic effects in comparing different data sets.

II. EXPERIMENTAL APPARATUS

A. The lead-glass array

The detector used in these measurements consisted of 245 blocks of SF5 lead glass ($n = 1.67$ at 589 nm), each having a square face measuring 14.5×14.5 cm^2. The length of each block was either 35 or 40 cm, correspond-

ing to 15 or 17 radiation lengths, respectively. These counters were fabricated in the mid 1970s and had previously been used in experments at the CERN ISR [11].

The blocks were arranged in a nearly 180° azimuthal array as shown in Fig. 1. The distance between centers of neighboring blocks was 15.0 cm. The front faces of all blocks lay in a plane perpendicular to the beam axis at a distance 3.0 m downstream of the target. The laboratory polar angles covered by the array were 9° to 32°. (Pseudorapidity coverage was 1.25 to 2.50, which is roughly centered about 1.72, the nucleon-nucleon center-of-mass rapidity at AGS energy.) Note that this array differs in geometry from the full 360° azimuthal array used in some earlier measurements of AGS Experiment 802 [3].

B. Calibration and response to electrons

A light pulser consisting of a 3 mm diameter, 1 mm thick CsI(Tl) scintillator and a ^{241}Am α-ray source was attached to the front of each lead-glass counter for the purpose of monitoring the gain [12]. These pulsers provided a constant reference signal available at all stages of calibration and running. During the data taking, special runs of CsI pulser data were taken periodically.

The gain of each lead-glass block was calibrated in a 2 GeV/c negative beam at the AGS, two years before the measurements reported here. Approximately 20% of the calibration beam was identified electrons, and the signals from these were used to find the photon-equivalent energy of the CsI pulsers. A detailed description of the entire calibration procedure may be found elsewhere [13]. The energy resolution, $\Delta E/E$, for photons and electrons was

TABLE I. Beams and targets used in the reported data. Additional nucleus-nucleus measurements with 1% (Si) interaction length targets produced identical results with those reported.

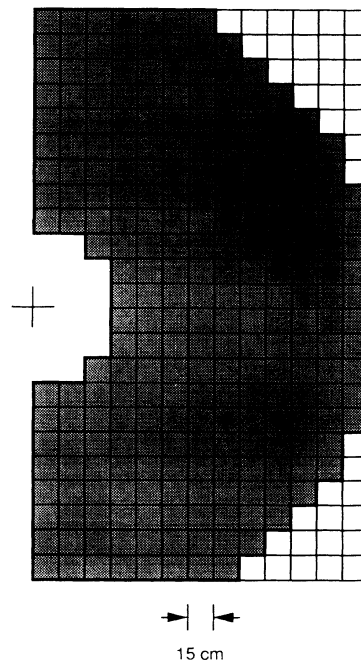| Beam(s)	Target	Thickness (mg/cm^2)	Percent of interaction length
p	Be	1480	2
p	C	474	1
p	Al	1630	2
O, Si	Al	817	3 (Si)
p, O, Si	Cu	1440	3 (Si)
O, Si	Ag	1946	3 (Si)
p, O, Si	Au	2939	3 (Si)

FIG. 1. Arrangement of the 245 lead-glass blocks to form an array covering half of the azimuthal angles. The cross hair marks the position of the beam axis, which goes into the page.

$6\%/\sqrt{E}$ to $8\%/\sqrt{E}$, where E is in GeV. The response of these counters to Čerenkov light was linear to $\pm 1\%$ for electrons [11].

All data in this paper were taken over a six month period during which time the systematic drifts in the energy scale of the calibration were well controlled, being of the order of a few percent. For details on this point, see Sec. IV.

C. Hadronic response and composition of the signal

Lead glass acts as a Čerenkov counter designed to measure deposited electromagnetic energy. It is sensitive to photons, typically produced by the reactions $\pi^0 \rightarrow \gamma\gamma$ and $\eta^0 \rightarrow \gamma\gamma$, and to direct electrons. However, there is a large response from the Čerenkov radiation of passing charged hadrons (for $\beta > \beta_c$, with the value of β_c nominally 0.6, but more realisitically 0.8), as well as some background from hadronic interactions in the lead glass.

Segmentation of the array was not sufficient to distinguish individual showers, and no attempt has been made to correct the energy measured in the lead glass on an event-by-event basis for the charged particle contribution. Therefore, the data are presented simply in terms of the total pulse-height equivalent energy observed in the detector.

Negative pions in the calibration beam were used to measure the hadronic response of the lead glass. It was found that the photon equivaient energy of 2 GeV/c π^- punching through the blocks was approximately 0.45 GeV for incident angles relevant for this detector [13]. No difference in the signal for muons and charged pions was observed, as expected for Čerenkov radiation.

The actual inclusive spectra of charged particles produced in Si+Au central collisions near midrapidity have been reported [14]. From these, an estimate of the charged hadron signal in the lead glass may be determined. Assuming the π^0 yield, as well as the π^0 mean transverse momentum, to be the average of that from π^+ and π^-, the electromagnetic contribution may also be estimated. The result of this calculation [15] shows that the mean contributions to the total lead-glass equivalent energy of neutral pions, charged pions, and protons are in the ratio of 11:7:1, respectively. In other words, at least 95% of the signal observed in the lead glass is due to produced particles (i.e., not nucleons). This basic conclusion is unchanged for the case of p+Be and p+Au collisions, based on the inclusive spectra from those systems [16].

D. Electronics and triggering

At the end of each lead-glass block was a 13-cm RCA 8055 photomultiplier tube. The signals, which were decoupled from the high voltage ground of the photomultipliers, were sent through 70 m of RG58 cable to the counting house where a high impedance tap was used for the trigger electronics. The signals then passed through remotely switchable $\times 5$ attenuators and were fed into LRS 1882 12-bit Fastbus ADC's through 460 ns long RG58 delay cables to allow time for the trigger to be

formed. The ADC gate width used was 300 ns for normal data collection, and 1.8 μs for CsI pulser measurements. The nominal value of the gains was 7 MeV per ADC channel. Special minimum bias runs with the attenuators removed were taken for the proton-nucleus collisions in order to study the spectra at the lowest values of E_T.

Two types of hardware triggers were used to select the events included in this data set. The first was a minimum-bias interaction trigger, INT, which was defined as a good beam particle in coincidence with a veto from a bulls-eye scintillator counter 10.6 m downstream of the target along the beam axis [17]. The threshold on the bulls-eye was set to veto charge states $Z \leq 0.7$ for the proton beam, $Z \leq 7$ for the O beam, and $Z \leq 12$ for the Si beam. The other trigger used, PB2, was a lead-glass self-trigger on high E_T. This was determined from a weighted analog sum of the photomultiplier outputs in groups of 16 channels each; the weighting factor of each group in the sum was given by the common value of $\langle \sin\theta \rangle$ for the group. An adjustable discriminator allowed the PB2 threshold to be set to the desired value.

E. Off-line data reduction and analysis

Some corrections to the data were applied off-line before combining the various data sets (INT, PB2) to form the final spectra. First, the gain of each channel was updated according to the CsI pulser run closest in time. Second, it was necessary to correct an observed common-mode pedestal shift problem which may have arisen from pickup in the signal cables in the counting house. On an event-by-event basis, the departures of the unhit channels from the nominal pedestal ADC values were calculated in groups of 16 channels on the same Fastbus ADC. Pedestals were then corrected by the average baseline shift of the group. To ensure being above the noise of the common-mode shift problem, a 50 MeV ($\approx$ 7 ADC channels) cut in equivalent energy was applied to each block before including it in the global sum. Thus the transverse energy, E_T^{PbGl}, was defined by

$$E_T^{\text{PbGl}} = \sum_{\text{blocks},\, E_i > 50\ \text{MeV}} E_i \sin\theta_i, \qquad (1)$$

where E_i is the energy in block i, θ_i is the polar angle from the beam axis to the center of the face of block i, and the sum is over all blocks, i, $1 \leq i \leq 245$, for which $E_i > 50$ MeV. Similarly, the total energy, $E_{\text{tot}}^{\text{PbGl}}$, was defined by

$$E_{\text{tot}}^{\text{PbGl}} = \sum_{\text{blocks},\, E_i > 50\ \text{MeV}} E_i. \qquad (2)$$

Only events for which $E_T^{\text{PbGl}} > 0$ (and hence $E_{\text{tot}}^{\text{PbGl}} > 0$) were included in the histograms. An increase in the hit-block threshold from 50 to 100 MeV leaves the results of this analysis unchanged for nucleus-nucleus spectra and decreases the absolute normalization of the proton-nucleus spectra by about 20%.

The third correction was a veto on any event which had beam counts in a 1 μs gate on either side of the event; this eliminated possible pileup. A fourth correction was

for the target-out effects of the target holder, beam pipe, etc. Target-out runs were collected regularly during the data taking, and the spectrum of counts per unit beam flux with an empty target holder was subtracted from the spectrum of counts per unit beam flux with the real target. For the case of the oxygen and silicon beams on 3% (Si) interaction length thick targets, this correction is important only in the lowest transverse energy bin ($E_T^{\mathrm{PbGl}} < 0.5$ GeV) where it ranges from 30 to 50% of the uncorrected value. In all higher E_T^{PbGl} bins for O+A and Si+A, the correction is totally negligible [18]. For proton beam spectra, the target-out correction is significant at all values of E_T^{PbGl} and ranges from 12 to 18% of the uncorrected cross section.

III. PRESENTATION OF THE GLOBAL TRANSVERSE ENERGY SPECTRA

A. Proton-nucleus spectra

Figure 2 shows the differential cross section in E_T^{PbGl} for the proton beam on four targets: beryllium, aluminum, copper, and gold. The data, along with values for a carbon target, are listed in Table II. (The p+C spectrum is very similar in shape to that of p+Be.) The data are plotted up to 2.5 GeV where the size of the pileup correction has been verified to be negligible. All spectra, except the carbon, include data from the special minimum bias runs with the ×5 attenuators removed (in which case the equivalent energy threshold for a "hit" block is 10 MeV rather than 50 MeV).

The qualitative similarity of the curves, for targets ranging from ^{9}Be to ^{197}Au, and for roughly five decades in cross section, is striking. Indeed, Fig. 3 shows that

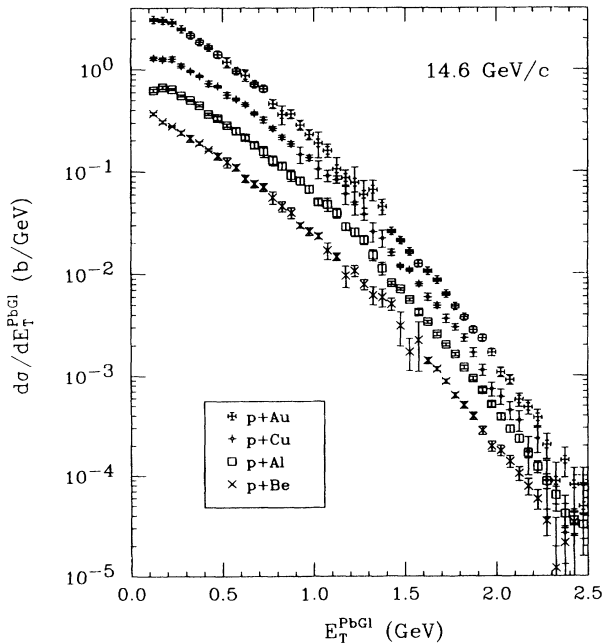the ratio $(d\sigma/dE_T^{\mathrm{PbGl}})_{p+\mathrm{Au}}/(d\sigma/dE_T^{\mathrm{PbGl}})_{p+A}$, where $A =$ Be, Al, or Cu, is approximately constant at all values of E_T^{PbGl}. For comparison, the geometric ratio $(197/A)^{2/3}$ is also shown; this is only slightly higher than the cross-section ratio at the highest E_T^{PbGl}. If target nucleons appear "black" to the projectile proton, then $d\sigma/dE_T^{\mathrm{PbGl}}$ is expected to be proportional to $A^{2/3}$. The general universality of $p+A$ spectra is not observed at $200A$ GeV/c at CERN [8].

Closer examination of the spectra at the lowest values of E_T^{PbGl}, however, reveals some differences among the targets. To quantify this, the average values of E_T^{PbGl} and $E_{\mathrm{tot}}^{\mathrm{PbGl}}$ were determined from fits to the spectra. Although a single gamma distribution was used in Ref. [3], better fits over the full five decades in cross section were obtained with the double gamma distribution:

$$\frac{d\sigma}{dE} = \sigma_{\mathrm{total}}\, b\left[\frac{\varepsilon}{\Gamma(p_1)}(bE)^{p_1-1} + \frac{(1-\varepsilon)}{\Gamma(p_2)}(bE)^{p_2-1}\right]e^{-bE},$$

$$(3)$$

where E is equal to E_T^{PbGl} or $E_{\mathrm{tot}}^{\mathrm{PbGl}}$, $\Gamma(p)$ is the gamma function, with $\Gamma(p) = (p-1)!$ if p is an integer, and the fit parameters are σ_{tot}, b, ε, p_1, and p_2. These fit parameters and the resulting mean values of E_T^{PbGl} and $E_{\mathrm{tot}}^{\mathrm{PbGl}}$, along with $\langle\sin\theta\rangle \equiv \langle E_T^{\mathrm{PbGl}}\rangle/\langle E_{\mathrm{tot}}^{\mathrm{PbGl}}\rangle$, are listed in Table III.

Table III shows that the mean E_T^{PbGl} increases from Be to Al is similar for Al and Cu, but actually decreases from Cu to Au. (The mean $E_{\mathrm{tot}}^{\mathrm{PbGl}}$ for p+Au is actually lower
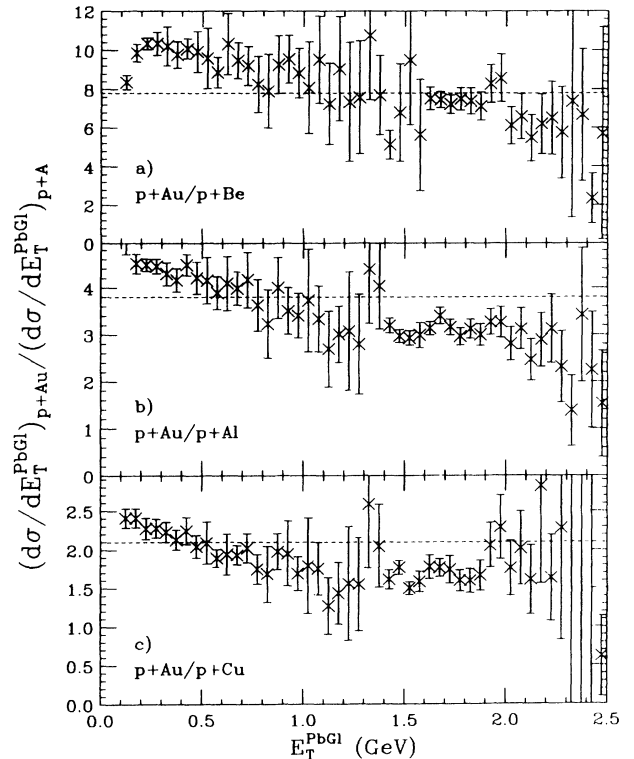

FIG. 2. The transverse energy spectra for $p + A$ reactions.

FIG. 3. The ratio of cross sections $(d\sigma/dE_T^{\mathrm{PbGl}})_{p+\mathrm{Au}}/(d\sigma/dE_T^{\mathrm{PbGl}})_{p+A}$. The dashed line shows the ratio $(197/A)^{2/3}$. (a) For target Be, (b) for target Al, and (c) for target Cu.

than that for all lighter targets, as has been previously pointed out [4, 15].) This fact presents a dilemma, since Au is the thickest target, and therefore p+Au reactions should involve more collisions (and hence higher mean transverse energy) than p+Cu.

A possible explanation is seen by looking at the angular dependence of the spectra. Fig. 4 shows the quantity $dE_T^{PbGl}/d\eta$ (per event) as a function of the pseudorapidity, η, for the four targets in two different slices of E_T^{PbGl}

that are on the high-energy tail of the distributions. A geometric acceptance correction has been applied to each of the eight pseudorapidity bins used, and the distribution is normalized to the half-coverage in azimuth by

$$\int_{\eta=1.25}^{\eta=2.50} \left[\frac{dE_T^{PbGl}}{d\eta} \right] d\eta = \langle E_T^{PbGl} \rangle_{E_T^{PbGl} \text{ slice}}, \qquad (4)$$

where $\langle E_T^{PbGl} \rangle_{E_T^{PbGl} \text{ slice}}$ is the mean value of E_T^{PbGl} in the

TABLE II. $d\sigma/dE_T^{PbGl}$ versus E_T^{PbGl} for $p + A$ reactions, in b/GeV, where NE-n denotes $N \times 10^{-n}$. Errors quoted are statistical only; systematic errors are estimated to be less than 5%.

E_T^{PbGl} (GeV)	p+Be	p+C	p+Al	p+Cu	p+Au
0.10-0.15	3.70E-1±1.11E-2		6.24E-1±2.32E-2	1.28E+0±5.10E-2	3.09E+0±9.90E-2
0.15-0.20	3.06E-1±1.01E-2		6.69E-1±2.30E-2	1.25E+0±4.81E-2	3.02E+0±9.50E-2
0.20-0.25	2.78E-1±5.48E-3	3.68E-1±1.37E-2	6.42E-1±1.28E-2	1.27E+0±6.93E-2	2.88E+0±6.30E-2
0.25-0.30	2.39E-1±1.18E-2	3.23E-1±1.26E-2	5.55E-1±1.19E-2	1.09E+0±4.89E-2	2.47E+0±6.98E-2
0.30-0.35	2.10E-1±1.73E-2	2.77E-1±1.15E-2	5.00E-1±1.12E-2	9.62E-1±2.36E-2	2.15E+0±1.13E-1
0.35-0.40	1.89E-1±8.08E-3	2.44E-1±1.07E-2	4.44E-1±1.05E-2	8.68E-1±2.22E-2	1.85E+0±1.00E-1
0.40-0.45	1.63E-1±4.13E-3	2.12E-1±9.89E-3	3.66E-1±9.53E-3	7.30E-1±4.63E-2	1.64E+0±7.23E-2
0.45-0.50	1.41E-1±1.14E-2	1.75E-1±9.03E-3	3.32E-1±1.60E-2	6.84E-1±1.95E-2	1.40E+0±9.15E-2
0.50-0.55	1.23E-1±1.40E-2	1.50E-1±8.34E-3	2.84E-1±1.01E-2	5.64E-1±3.62E-2	1.18E+0±1.34E-1
0.55-0.60	1.09E-1±7.72E-3	1.45E-1±7.95E-3	2.49E-1±1.78E-2	5.12E-1±1.67E-2	9.68E-1±5.08E-2
0.60-0.65	8.51E-2±6.78E-3	1.13E-1±7.11E-3	2.15E-1±1.24E-2	4.52E-1±1.99E-2	8.78E-1±1.12E-1
0.65-0.70	7.59E-2±6.11E-3	1.11E-1±6.81E-3	1.80E-1±1.27E-2	3.72E-1±1.42E-2	7.19E-1±3.83E-2
0.70-0.75	7.04E-2±6.01E-3	7.82E-2±5.89E-3	1.56E-1±1.96E-2	3.21E-1±2.09E-2	6.49E-1±4.26E-2
0.75-0.80	5.60E-2±7.93E-3	6.30E-2±5.30E-3	1.28E-1±1.42E-2	2.64E-1±1.19E-2	4.62E-1±4.71E-2
0.80-0.85	4.60E-2±5.36E-3	5.31E-2±4.84E-3	1.13E-1±9.32E-3	2.15E-1±1.07E-2	3.64E-1±7.62E-2
0.85-0.90	3.95E-2±4.81E-3	5.34E-2±4.66E-3	9.14E-2±1.15E-2	1.85E-1±1.03E-2	3.66E-1±3.77E-2
0.90-0.95	2.99E-2±1.81E-3	4.35E-2±4.21E-3	8.14E-2±7.02E-3	1.46E-1±2.66E-2	2.85E-1±3.23E-2
0.95-1.00	2.60E-2±2.25E-3	3.31E-2±3.71E-3	6.74E-2±5.26E-3	1.35E-1±8.40E-3	2.30E-1±2.64E-2
1.00-1.05	2.33E-2±1.53E-3	2.95E-2±3.45E-3	5.04E-2±3.67E-3	1.05E-1±2.03E-2	1.88E-1±5.36E-2
1.05-1.10	1.68E-2±3.05E-3	2.08E-2±2.97E-3	4.79E-2±7.20E-3	9.10E-2±1.14E-2	1.60E-1±2.37E-2
1.10-1.15	1.46E-2±1.21E-3	1.80E-2±2.73E-3	3.92E-2±4.43E-3	8.31E-2±6.52E-3	1.06E-1±2.94E-2
1.15-1.20	9.58E-3±2.27E-3	1.13E-2±2.28E-3	2.88E-2±2.60E-3	6.04E-2±1.30E-2	8.66E-2±1.55E-2
1.20-1.25	1.07E-2±1.34E-3	6.26E-3±1.85E-3	2.56E-2±2.43E-3	5.02E-2±1.28E-2	7.86E-2±3.13E-2
1.25-1.30	7.87E-3±8.92E-4	9.72E-3±2.00E-3	2.13E-2±2.22E-3	3.84E-2±5.27E-3	5.96E-2±2.18E-2
1.30-1.35	6.21E-3±1.24E-3	8.27E-3±1.83E-3	1.52E-2±1.89E-3	2.58E-2±5.62E-3	6.67E-2±1.53E-2
1.35-1.40	5.92E-3±1.20E-3	3.26E-3±1.34E-3	1.13E-2±1.65E-3	2.22E-2±4.34E-3	4.55E-2±7.84E-3
1.40-1.45	5.06E-3±7.09E-4	5.55E-3±1.49E-3	8.11E-3±2.93E-4	1.61E-2±1.13E-3	2.59E-2±8.57E-4
1.45-1.50	3.09E-3±1.14E-3	4.58E-3±1.35E-3	7.07E-3±1.99E-4	1.19E-2±4.29E-4	2.10E-2±7.70E-4
1.50-1.55	1.72E-3±5.97E-4	9.04E-4±8.56E-4	5.57E-3±1.77E-4	1.09E-2±4.03E-4	1.63E-2±6.81E-4
1.55-1.60	2.23E-3±1.13E-3	4.05E-3±1.21E-3	4.20E-3±2.31E-4	7.91E-3±3.58E-4	1.25E-2±8.95E-4
1.60-1.65	1.41E-3±1.01E-4	2.38E-3±9.76E-4	3.38E-3±1.17E-4	5.95E-3±4.83E-4	1.06E-2±3.21E-4
1.65-1.70	1.16E-3±5.30E-5	1.57E-4±5.49E-4	2.55E-3±1.05E-4	4.91E-3±2.76E-4	8.69E-3±2.91E-4
1.70-1.75	8.80E-4±4.63E-5	1.07E-3±7.02E-4	2.01E-3±7.10E-5	3.64E-3±3.48E-4	6.36E-3±2.52E-4
1.75-1.80	6.39E-4±3.99E-5	9.09E-4±6.40E-4	1.62E-3±6.54E-5	3.00E-3±2.17E-4	4.80E-3±2.22E-4
1.80-1.85	5.07E-4±3.82E-5	9.89E-4±6.30E-4	1.20E-3±4.66E-5	2.35E-3±1.93E-4	3.75E-3±1.97E-4
1.85-1.90	3.94E-4±3.18E-5		9.37E-4±4.12E-5	1.69E-3±1.70E-4	2.81E-3±1.78E-4
1.90-1.95	2.84E-4±2.72E-5		7.19E-4±3.66E-5	1.14E-3±1.41E-4	2.35E-3±1.57E-4
1.95-2.00	1.97E-4±2.31E-5		5.17E-4±3.16E-5	7.37E-4±1.18E-4	1.69E-3±1.35E-4
2.00-2.05	1.78E-4±2.15E-5		3.88E-4±2.77E-5	6.17E-4±1.07E-4	1.09E-3±1.14E-4
2.05-2.10	1.39E-4±1.92E-5		2.93E-4±2.46E-5	4.53E-4±9.33E-5	9.14E-4±1.04E-4
2.10-2.15	1.05E-4±1.68E-5		2.34E-4±2.19E-5	3.57E-4±8.34E-5	5.77E-4±8.73E-5
2.15-2.20	7.83E-5±1.48E-5		1.68E-4±1.92E-5	1.72E-4±7.15E-5	4.85E-4±7.93E-5
2.20-2.25	5.87E-5±1.30E-5		1.22E-4±1.69E-5	2.34E-4±6.70E-5	3.82E-4±7.15E-5
2.25-2.30	3.52E-5±1.05E-5		8.77E-5±1.46E-5	8.90E-5±5.07E-5	2.03E-4±5.74E-5
2.30-2.35	1.20E-5±7.66E-5		6.43E-5±1.28E-5	2.32E-6±3.56E-5	8.87E-5±4.50E-5
2.35-2.40	2.15E-5±8.35E-6		4.18E-5±1.07E-5	2.68E-5±3.61E-5	1.43E-4±4.72E-5
2.40-2.45	3.44E-5±9.42E-6		3.59E-5±9.93E-6	3.03E-6±2.89E-5	8.09E-5±3.83E-5
2.45-2.50	8.73E-6±5.93E-6		3.26E-5±9.22E-6	8.01E-5±3.94E-5	4.97E-5±3.39E-5

TABLE III. Summary of fits of $p+A$ $d\sigma/dE_T^{\rm PbGl}$ spectra to the form of Eq. (3). The cut $0.1 < E_T^{\rm PbGl} < 2.0$ GeV is used. $(0.4 < E_{\rm tot}^{\rm PbGl} < 7.2$ GeV for the $E_{\rm tot}^{\rm PbGl}$ fit.)

	$p+$Be	$p+$Al	$p+$Cu	$p+$Au
$\sigma_{\rm tot}$ (mb)	168 ± 7	333 ± 5	671 ± 14	1496 ± 25
ϵ (%)	67.9 ± 3.0	75.2 ± 1.8	67.8 ± 3.7	73.8 ± 8.6
b (GeV^{-1})	6.82 ± 0.27	7.46 ± 0.21	7.29 ± 0.31	6.44 ± 0.35
p_1	1.47 ± 0.17	2.14 ± 0.10	1.95 ± 0.17	1.74 ± 0.21
p_2	4.06 ± 0.34	5.06 ± 0.27	4.55 ± 0.39	3.64 ± 0.52
$\chi^2/$d.o.f.	$21/33$	$25/33$	$31/33$	$25/33$
$\langle E_T^{\rm PbGl}\rangle$ (GeV)	0.337 ± 0.010	0.384 ± 0.003	0.382 ± 0.006	0.347 ± 0.006
$\langle E_{\rm tot}^{\rm PbGl}\rangle$ (GeV)	1.22 ± 0.05	1.29 ± 0.04	1.33 ± 0.03	1.19 ± 0.02
$\langle\sin\theta\rangle \equiv$ $\langle E_T^{\rm PbGl}\rangle/\langle E_{\rm tot}^{\rm PbGl}\rangle$	0.276 ± 0.014	0.298 ± 0.010	0.287 ± 0.008	0.292 ± 0.007

slice. (This is a slice in $E_T^{\rm PbGl}$, not η.) The distributions all show a peak inside the detector acceptance, and, for a given slice, the differences from target to target are small. In summary, for events with $E_T^{\rm PbGl} > 1.0$ GeV and for all targets, the $dE_T^{\rm PbGl}/d\eta$ distribution peaks in the pseudorapidity range 1.5–1.7, well within the detector acceptance.

This is to be compared to Fig. 5, the same plots for the slice $0.2 < E_T^{\rm PbGl} < 0.3$ GeV. This slice is near the peak of the $d\sigma/dE_T^{\rm PbGl}$ spectra and most of the total cross section is nearby. The shape of the $dE_T^{\rm PbGl}/d\eta$ distribution progresses from a fairly flat $p+$Be to a backward sloped $p+$Au.

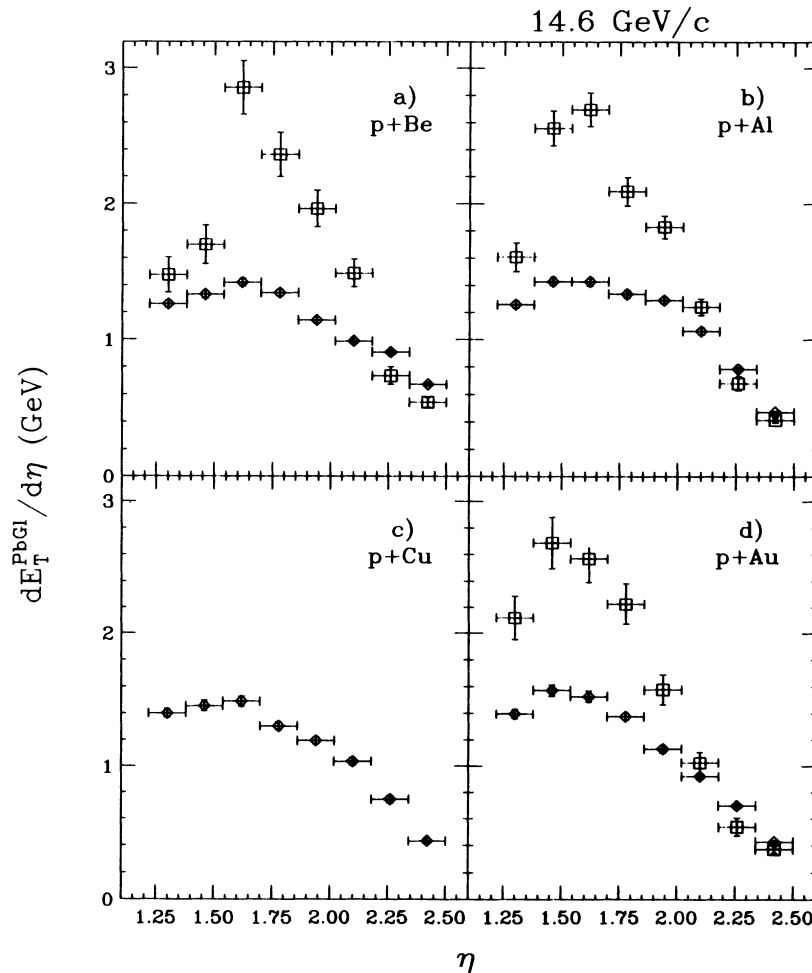The $dE_T^{\rm PbGl}/d\eta$ distribution for events with low $E_T^{\rm PbGl}$

FIG. 4. $dE_T^{\rm PbGl}/d\eta$ for $p + A$ reactions. The diamond-shaped points are for the slice $1.4 < E_T^{\rm PbGl} < 1.5$ GeV; the square points are for the slice $2.0 < E_T^{\rm PbGl} < 2.2$ GeV. The square points for $p+$Cu are not shown due to insufficient counting statistics. (a) $p+$Be, (b) $p+$Al, (c) $p+$Cu, and (d) $p+$Au

reproduces the shape of the minimum-bias dN/dy distributions for charged pions reported from the E802 spectrometer [16]. The spectrometer distributions show a very gentle peak for $p+\text{Be} \rightarrow \pi^{\pm} + X$ at $y \approx 1.7$ and a more pronounced peak for $p + \text{Au} \rightarrow \pi^{\pm} + X$ at $y \approx 0.9$, well outside the lead-glass detector acceptance. Thus, the large cross section for events at low E_T^{PbGl} found in $p+\text{Au}$ which causes $\langle E_T^{\text{PbGl}} \rangle_{p+\text{Au}} < \langle E_T^{\text{PbGl}} \rangle_{p+\text{Al,Cu}}$ is associated with a class of events where the pion distribution shifts backward by 0.8 unit of rapidity, leaving little energy in the midrapidity acceptance of the lead glass. In other words, the lead-glass acceptance does not cover the peak of the $dE_T^{\text{PbGl}}/d\eta$ distribution for low values of E_T^{PbGl} in $p+\text{Au}$, in contrast to other targets and higher values of E_T^{PbGl}.

B. Nucleus-nucleus spectra

The $d\sigma/dE_T^{\text{PbGl}}$ spectra for ^{16}O projectiles on targets of Al, Cu, Ag, and Au are shown in Fig. 6; spectra for ^{28}Si on the same targets are shown in Fig. 7. Numerical values are listed in Tables IV and V. Both sets of curves show the same general features: there is a "plateau" region corresponding to peripheral reactions, followed by a "knee" where the curve turns over, and finally an ex-

ponential tail at high transverse energy, corresponding to the most central reactions. For the aluminum target the plateau region barely exists, and the curve turns over at lower energy. The high-energy tails, for all targets of copper and heavier, display similar behavior at the "end point" of the transverse energy.

Following Fig. 3, we explore the apparent transverse energy saturation in Fig. 8. The top part [Fig. 8(a)] shows the ratio $(d\sigma/dE_T^{\text{PbGl}})_{\text{O}+\text{Au}}/(d\sigma/dE_T^{\text{PbGl}})_{\text{O}+A}$, and the bottom part [Fig. 8(b)] shows $(d\sigma/dE_T^{\text{PbGl}})_{\text{Si}+\text{Au}}/(d\sigma/dE_T^{\text{PbGl}})_{\text{Si}+A}$, where $A = \text{Al, Cu}$, or Ag. For both the O and Si projectiles, the data show an unsaturated Au/Al ratio, Au/Cu beginning to saturate at the highest E_T^{PbGl}, and Au/Ag remaining constant over the entire high-energy tail. For comparison the dashed lines show the central geometric ratios given by

$$\left(\frac{197^{1/3} - A_{\text{proj}}^{1/3}}{A_{\text{targ}}^{1/3} - A_{\text{proj}}^{1/3}} \right)^2, \tag{5}$$

where A_{proj} is the mass number of the projectile, and A_{targ} is the mass number of the target being compared to ^{197}Au. The above expression is the ratio of geometric areas when the nuclei are considered as hard spheres and
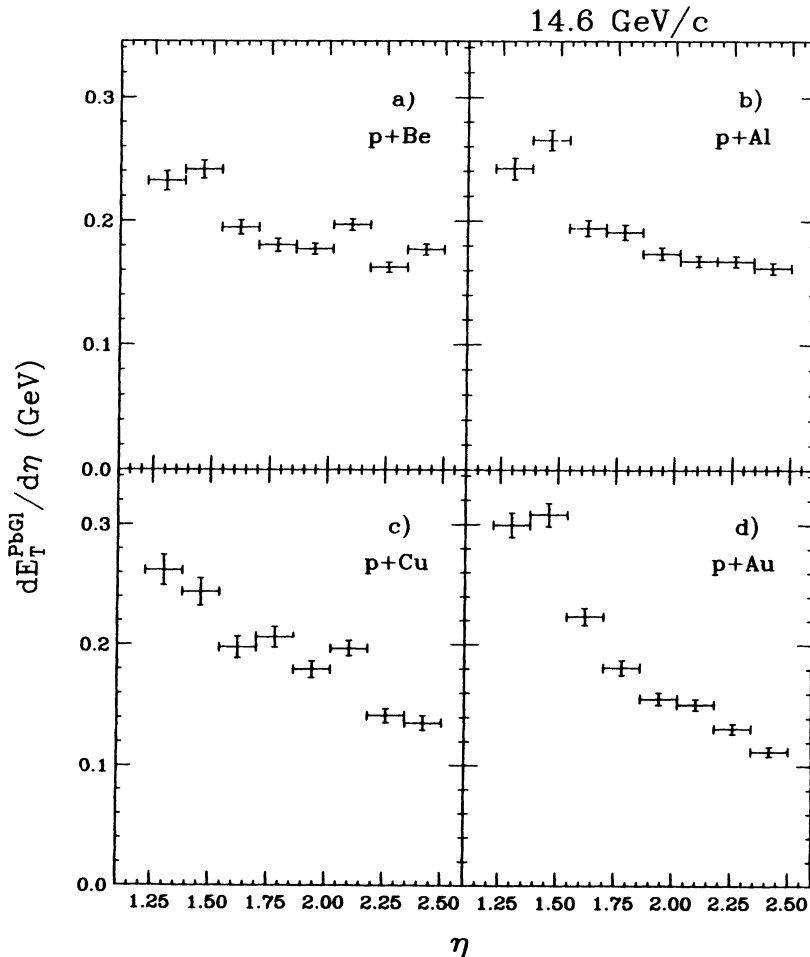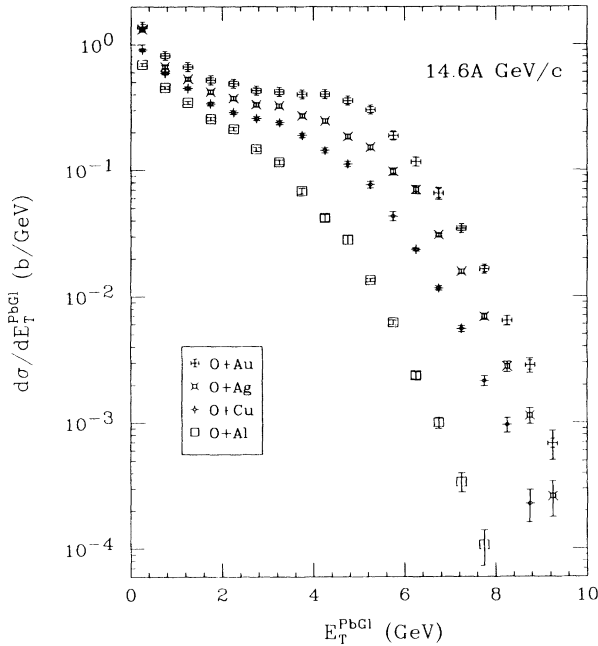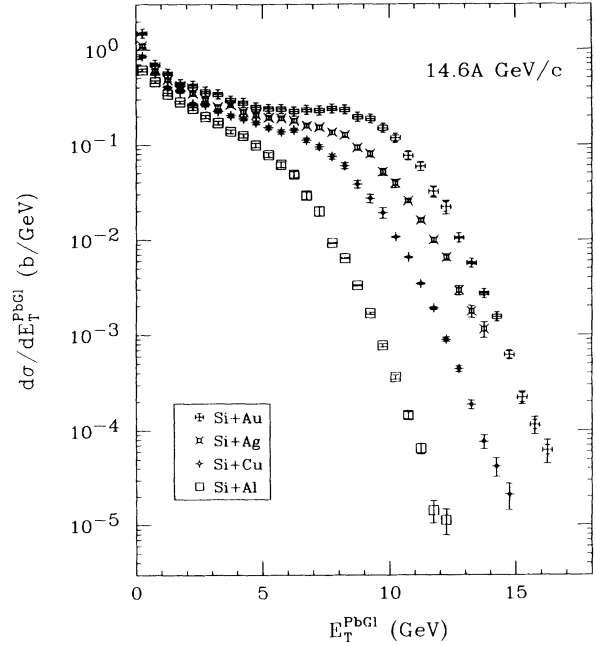

14.6 GeV/c

FIG. 5. $dE_T^{\text{PbGl}}/d\eta$ in the slice $0.2 < E_T^{\text{PbGl}} < 0.3$ GeV. (a) $p+$Be, (b) $p+$Al, (c) $p+$Cu, and (d) $p+$Au.

FIG. 6.　Transverse energy spectra for ^{16}O+A.

FIG. 7.　Transverse energy spectra for ^{28}Si+A.

the projectile nucleus fits completely inside the target nucleus. These data show the Au/Ag ratio saturating close to this value, while the Au/Cu overshoots somewhat.

A saturated ratio indicates that $d\sigma/dE_T^{PbGl}$ has the same shape for both of the targets (Au and Ag, or Au and Cu) above some value of E_T^{PbGl}; i.e., for the most central collisions, the transverse energy emission is the same for all heavy targets in spite of the differences in target nuclei thickness. It should be noted that an unsaturated ratio

may be explained in at least two different ways. First, if a colliding system is symmetric, or nearly symmetric as is the case in Si+Al, then geometry dictates that a large part of the projectile interacts only peripherally with the target, and much of the potential particle production is not realized. The second explanation for an unsaturated ratio is less trivial: if the nuclear matter of the target appears transparent to the projectile, even a target much thicker than the projectile will not saturate the particle

TABLE IV.　$d\sigma/dE_T^{PbGl}$ versus E_T^{PbGl} for O+A reactions, in b/GeV, where NE-n denotes $N \times 10^{-n}$. Errors quoted are statistical only; systematic errors are estimated to be less than 5%.

E_T^{PbGl} (GeV)	O+Al	O+Cu	O+Ag	O+Au
0.0–0.5	6.92E-1 ± 1.84E-2	9.10E-1 ± 2.64E-2	1.32E+0 ± 3.57E-2	1.40E+0 ± 6.37E-2
0.5–1.0	4.54E-1 ± 1.15E-2	5.92E-1 ± 1.66E-2	6.67E-1 ± 2.04E-2	8.18E-1 ± 3.60E-2
1.0–1.5	3.44E-1 ± 9.30E-3	4.47E-1 ± 1.35E-2	5.29E-1 ± 1.70E-2	6.62E-1 ± 2.96E-2
1.5–2.0	2.56E-1 ± 7.62E-3	3.37E-1 ± 1.12E-2	4.18E-1 ± 1.45E-2	5.19E-1 ± 2.44E-2
2.0–2.5	2.13E-1 ± 6.76E-3	2.88E-1 ± 1.01E-2	3.72E-1 ± 1.33E-2	4.88E-1 ± 2.30E-2
2.5–3.0	1.47E-1 ± 5.48E-3	2.58E-1 ± 9.32E-3	3.32E-1 ± 1.23E-2	4.29E-1 ± 2.09E-2
3.0–3.5	1.16E-1 ± 4.67E-3	2.41E-1 ± 8.73E-3	3.26E-1 ± 1.19E-2	4.20E-1 ± 2.02E-2
3.5–4.0	6.81E-2 ± 3.61E-3	1.90E-1 ± 7.75E-3	2.72E-1 ± 1.08E-2	4.02E-1 ± 1.97E-2
4.0–4.5	4.19E-2 ± 2.77E-3	1.44E-1 ± 6.62E-3	2.47E-1 ± 1.02E-2	4.02E-1 ± 1.96E-2
4.5–5.0	2.82E-2 ± 2.25E-3	1.12E-1 ± 5.80E-3	1.85E-1 ± 8.75E-3	3.57E-1 ± 1.82E-2
5.0–5.5	1.35E-2 ± 3.91E-4	7.63E-2 ± 4.73E-3	1.52E-1 ± 7.87E-3	3.03E-1 ± 1.64E-2
5.5–6.0	6.17E-3 ± 2.60E-4	4.31E-2 ± 3.52E-3	9.74E-2 ± 6.25E-3	1.88E-1 ± 1.25E-2
6.0–6.5	2.38E-3 ± 1.60E-4	2.35E-2 ± 6.69E-4	6.98E-2 ± 5.26E-3	1.17E-1 ± 9.59E-3
6.5–7.0	1.00E-3 ± 1.04E-4	1.16E-2 ± 4.62E-4	3.08E-2 ± 8.94E-4	6.52E-2 ± 7.04E-3
7.0–7.5	3.41E-4 ± 6.04E-5	5.53E-3 ± 3.16E-4	1.58E-2 ± 6.31E-4	3.46E-2 ± 1.45E-3
7.5–8.0	1.07E-4 ± 3.38E-5	2.15E-3 ± 1.96E-4	6.88E-3 ± 4.13E-4	1.66E-2 ± 9.31E-4
8.0–8.5		9.60E-4 ± 1.31E-4	2.79E-3 ± 2.62E-4	6.39E-3 ± 5.57E-4
8.5–9.0		2.28E-4 ± 6.58E-5	1.14E-3 ± 1.67E-4	2.86E-3 ± 3.65E-4
9.0–9.5			2.61E-4 ± 8.27E-5	6.83E-4 ± 1.77E-4
σ_{tot} (b)	1.192 ± 0.014	1.841 ± 0.021	2.522 ± 0.028	3.316 ± 0.050

production.

The boundedness of the cross-section ratios in Fig. 8 for targets of Cu and heavier is in contrast to the behavior at the higher energies of the CERN SPS. Many groups have reported results on the transverse energy at CERN [6–9], but the most appropriate comparison to the data presented here is with the NA35 Ring Calorimeter [7, 8], which has a similar coverage in pseudorapidity relative to the nucleon-nucleon center of mass. At $200A$ GeV, the NA35 results show the ratio $[(d\sigma/dE_T)_{\rm O+Au}/(d\sigma/dE_T)_{\rm O+Ag}] > 10$ and the ratio $[(d\sigma/dE_T)_{\rm O+Au}/(d\sigma/dE_T)_{\rm O+Cu}] \gg 10$ for the highest values of E_T, and continuing to rise.

The $dE_T^{\rm PbGl}/d\eta$ distributions for the four targets are shown in Figs. 9 and 10 in slices on the "plateau" ($2.0 < E_T^{\rm PbGl} < 2.5$ GeV for O+A, $5.0 < E_T^{\rm PbGl} < 5.5$ GeV for Si+A), near the "knee" ($5.0 < E_T^{\rm PbGl} < 5.5$ GeV for O+A, $9.0 < E_T^{\rm PbGl} < 9.5$ GeV for Si+A), and farther out on the tail ($8.0 < E_T^{\rm PbGl} < 8.5$ GeV for O+A, $13.0 < E_T^{\rm PbGl} < 13.5$ GeV for Si+A.) These plots are normalized as in Eq. (4); further discussion follows in Sec. V.

IV. ENERGY SCALE STABILITY OVER TIME

All of the data sets introduced above were taken during different running periods, each of approximately one month duration: the oxygen data were taken in June 1988, the proton data in November 1988, and the silicon data in December 1988. In order to make comparisons across data sets it is important to first understand the stability of the detector's energy scale over time.

Previous preliminary measurements performed with the same lead-glass array have been reported from the AGS silicon beam runs of April 1987 [4] and December 1987 [19]. The older spectra for Si+Al and Si+Au are compared to the present (December 1988) result in Fig. 11. Note that the energy scale for the 245 block array given in Ref. [4] is missing a factor of 1.045 due to a calculation error in the calibration, and that the April 1987 data in Fig. 11 have been corrected for this. The Si+Au spectra from April 1987 and December 1988 agree very well, while the Si+Al spectrum from April 1987 is consistent with a downward scale change of 3%

TABLE V. $d\sigma/dE_T^{\rm PbGl}$ versus $E_T^{\rm PbGl}$ for Si+A reactions, in b/GeV, where NE-n denotes $N \times 10^{-n}$. Errors quoted are statistical only; systematic errors are estimated to be less than 5%.

$E_T^{\rm PbGl}$ (GeV)	Si+Al	Si+Cu	Si+Ag	Si+Au
0.0–0.5	6.09E-1 ± 2.37E-2	8.56E-1 ± 3.24E-2	1.11E+0 ± 4.18E-2	1.50E+0 ± 5.49E-2
0.5–1.0	4.58E-1 ± 1.31E-2	5.61E-1 ± 1.68E-2	6.07E-1 ± 2.03E-2	7.03E-1 ± 2.57E-2
1.0–1.5	3.40E-1 ± 1.08E-2	4.04E-1 ± 1.37E-2	4.81E-1 ± 1.74E-2	5.63E-1 ± 2.22E-2
1.5–2.0	2.82E-1 ± 9.54E-3	3.64E-1 ± 1.26E-2	4.18E-1 ± 1.57E-2	4.35E-1 ± 1.90E-2
2.0–2.5	2.43E-1 ± 8.71E-3	2.74E-1 ± 1.08E-2	3.49E-1 ± 1.42E-2	4.22E-1 ± 1.84E-2
2.5–3.0	1.99E-1 ± 7.77E-3	2.65E-1 ± 1.04E-2	3.02E-1 ± 1.30E-2	3.64E-1 ± 1.68E-2
3.0–3.5	1.71E-1 ± 7.14E-3	2.28E-1 ± 9.56E-3	2.53E-1 ± 1.18E-2	3.42E-1 ± 1.61E-2
3.5–4.0	1.39E-1 ± 6.37E-3	2.05E-1 ± 8.93E-3	2.67E-1 ± 1.18E-2	2.96E-1 ± 1.48E-2
4.0–4.5	1.25E-1 ± 5.98E-3	1.89E-1 ± 8.48E-3	2.23E-1 ± 1.08E-2	2.78E-1 ± 1.42E-2
4.5–5.0	9.99E-2 ± 5.29E-3	1.73E-1 ± 7.99E-3	2.07E-1 ± 1.02E-2	2.51E-1 ± 1.33E-2
5.0–5.5	7.87E-2 ± 4.66E-3	1.53E-1 ± 7.42E-3	1.94E-1 ± 9.74E-3	2.41E-1 ± 1.29E-2
5.5–6.0	6.20E-2 ± 4.05E-3	1.38E-1 ± 6.89E-3	1.91E-1 ± 9.45E-3	2.40E-1 ± 1.26E-2
6.0–6.5	4.88E-2 ± 3.58E-3	1.44E-1 ± 6.99E-3	1.81E-1 ± 9.13E-3	2.27E-1 ± 1.21E-2
6.5–7.0	2.91E-2 ± 2.72E-3	1.13E-1 ± 6.06E-3	1.60E-1 ± 8.43E-3	2.35E-1 ± 1.22E-2
7.0–7.5	2.00E-2 ± 2.29E-3	9.60E-2 ± 5.58E-3	1.54E-1 ± 8.27E-3	2.31E-1 ± 1.21E-2
7.5–8.0	9.29E-3 ± 9.90E-5	7.55E-2 ± 4.86E-3	1.36E-1 ± 7.66E-3	2.41E-1 ± 1.22E-2
8.0–8.5	6.39E-3 ± 8.15E-5	6.00E-2 ± 4.35E-3	1.27E-1 ± 7.41E-3	2.35E-1 ± 1.21E-2
8.5–9.0	3.32E-3 ± 5.83E-5	3.82E-2 ± 3.43E-3	9.34E-2 ± 6.29E-3	1.97E-1 ± 1.10E-2
9.0–9.5	1.68E-3 ± 4.14E-5	2.71E-2 ± 2.86E-3	8.05E-2 ± 5.81E-3	1.89E-1 ± 1.07E-2
9.5–10.0	7.79E-4 ± 2.81E-5	1.92E-2 ± 2.40E-3	5.17E-2 ± 4.63E-3	1.51E-1 ± 9.51E-3
10.0–10.5	3.62E-4 ± 1.91E-5	1.08E-2 ± 1.54E-4	3.91E-2 ± 4.02E-3	1.18E-1 ± 8.39E-3
10.5–11.0	1.44E-4 ± 1.21E-5	6.52E-3 ± 1.18E-4	2.54E-2 ± 9.79E-4	7.65E-2 ± 6.72E-3
11.0–11.5	6.48E-5 ± 8.10E-6	3.45E-3 ± 8.56E-5	1.60E-2 ± 7.74E-4	5.91E-2 ± 5.89E-3
11.5–12.0	1.42E-5 ± 3.79E-6	1.90E-3 ± 6.33E-5	9.97E-3 ± 6.10E-4	3.19E-2 ± 4.31E-3
12.0–12.5	1.12E-5 ± 3.36E-6	8.95E-4 ± 4.33E-5	6.52E-3 ± 4.93E-4	2.20E-2 ± 3.58E-3
12.5–13.0		4.43E-4 ± 3.05E-5	2.93E-3 ± 3.30E-4	1.05E-2 ± 2.25E-4
13.0–13.5		1.86E-4 ± 1.97E-5	1.76E-3 ± 2.55E-4	5.66E-3 ± 1.64E-4
13.5–14.0		7.62E-5 ± 1.26E-5	1.14E-3 ± 2.16E-4	2.71E-3 ± 1.14E-4
14.0–14.5		4.21E-5 ± 9.42E-6		1.54E-3 ± 8.57E-5
14.5–15.0		2.11E-5 ± 6.66E-6		6.21E-4 ± 5.43E-5
15.0–15.5				2.21E-4 ± 3.24E-5
15.5–16.0				1.15E-4 ± 2.34E-5
16.0–16.5				6.21E-5 ± 1.72E-5
$\sigma_{\rm tot}$ (b)	1.463 ± 0.018	2.204 ± 0.025	2.844 ± 0.032	3.835 ± 0.044
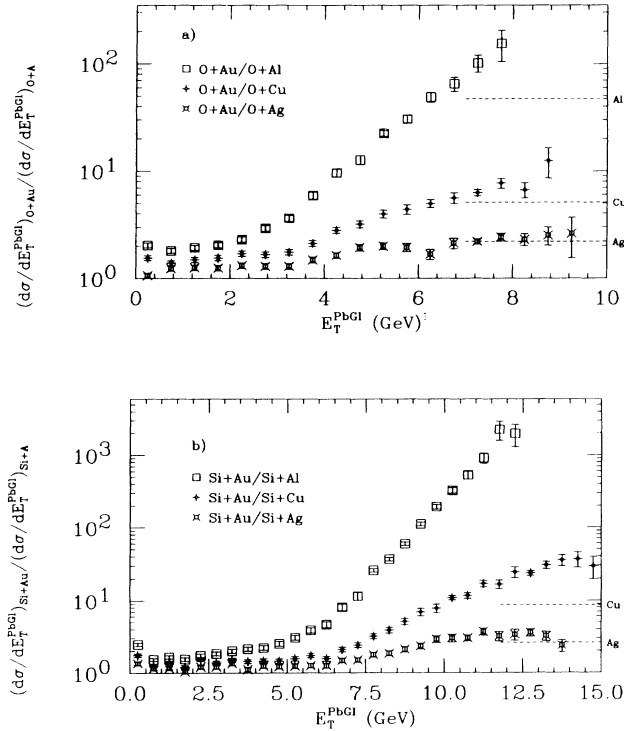
FIG. 8. The ratio of cross sections $(d\sigma/dE_T^{PbGl})_{Au}/$ $(d\sigma/dE_T^{PbGl})_A$ for A = Al, Cu, and Ag. The dashed line shows the central geometric ratio $[(197^{1/3} - A_{proj}^{1/3})/(A_{targ}^{1/3} - A_{proj}^{1/3})]^2$. (a) For projectile ^{16}O, (b) for projectile ^{28}Si.

from December 1988. The December 1987 spectra for both Si+Al and Si+Au appear approximately 3% higher in energy scale than December 1988. We conclude that the energy scale does indeed fluctuate on the order of a few percent over periods of six months to a year, and we assign an error to the relative energy scale among targets within a set from a given month of ±1.5%.

V. CHARACTERIZATION OF THE PSEUDORAPIDITY DISTRIBUTIONS

From Figs. 4, 9, and 10, it appears that the peaks of all angular distributions $dE_T^{PbGl}/d\eta$ are inside the lead-glass acceptance. (Exceptions to this are the proton-nucleus spectra at very low values of E_T^{PbGl}, as shown in Fig. 5.) It is thus unlikely that the saturation of cross-section ratios observed in Figs. 3 and 8 is due to an effect of the detector acceptance. This argument can be quantified as follows.

A proper description of the $dE_T^{PbGl}/d\eta$ distribution would require the full coverage in pseudorapidity; however, a good characterization may be made by fits to a Gaussian form [20]. Table VI lists the results of fits of the experimental distributions in successive E_T^{PbGl} slices to the formula

$$\left(\frac{dE_T^{PbGl}}{d\eta}\right)_{fit} = \rho \exp\left[\frac{-(\eta - \eta_0)^2}{2\ s^2}\right], \tag{6}$$

where ρ, η_0, and s are the fit parameters. Note that Eq. (6) is normalized such that

$$\int_{-\infty}^{\infty} \left(\frac{dE_T^{PbGl}}{d\eta}\right)_{fit} d\eta = \rho\ s\sqrt{2\pi} = E_T^{all\ \eta}, \tag{7}$$

where $E_T^{all\ \eta}$ is the total transverse energy (for the half-arc in azimuth) over all pseudorapidity, as extrapolated by the fit. The distributions for E_T^{PbGl} slices below 1 GeV (as shown for the $p+A$ cases in Fig. 5) are not well described by Gaussians.

Several trends are apparent from Table VI. First, the peak height, ρ, is roughly proportional to E_T^{PbGl}. Figure 12(a) shows that systematic variations in ρ/E_T^{PbGl} from target to target are of the order of 5–10 %. Second, the peak position, η_0, for a given projectile and target does not change with changing E_T^{PbGl} for $E_T^{PbGl} > 5$ GeV. This is shown in Fig. 12(b) and is in contrast to the case reported by the HELIOS Collaboration [21] for S+W at $200A$ GeV. Given the same Si projectile, the value of η_0 is lower for heavier targets, consistent with a shifting "backward" of the center of mass. For the case of Si+Au, the value of η_0 is consistent with the peak rapidity for charged pions found by the E802 spectrometer [14], namely, 1.46.

Next, Fig. 12(c) shows that the rms width, s, decreases slowly with increasing E_T^{PbGl}. The values for s are similar for all O+A and Si+A reactions, but are lower for $p+A$ ($s < 0.5$ for $E_T^{PbGl} > 1.5$ GeV.) The value $s = 1.02 \pm 0.03$ that has been previously reported [20] for the pseudorapidity distribution of all charged secondaries from O+Ag,Br at $14.6A$ GeV is consistent with these results.

Finally, the information gained from these fits may be used to study the effect of detector acceptance on the shapes of the $d\sigma/dE_T^{PbGl}$ spectra. From Eq. (7), the total transverse energy extrapolated over all pseudorapidity is proportional to ρs. For any given projectile and fixed E_T^{PbGl}, systematic differences in ρs between the different targets are less than or equal to 15%. It is, however, difficult to draw any conclusions from an extrapolation outside the detector acceptance, since any such conclusion would be model dependent.

It is possible to define an acceptance-independent cross section for transverse energy distributions without measuring the total emitted E_T over all pseudorapidity. Since the maximum of the $dE_T/d\eta$ distribution remains within our detector acceptance for all cases, the height of the maximum, ρ, provides a measurable quantity characteristic of the global transverse energy flow. It is, in fact, the quantity proposed by Bjorken [1] as the estimator of the energy density. (In analogy to proton-proton collisions it corresponds to using $[dn/dy]_{y_{NN}}$ to characterize the multiplicity distribution instead of the total multiplicity over all rapidity.) The differential cross section in $\rho = [dE_T^{PbGl}/d\eta]_{\eta_0}$ is shown as a function of ρ in Fig. 13(a) for O+Al,Cu,Ag,Au and in Fig. 13(b) for
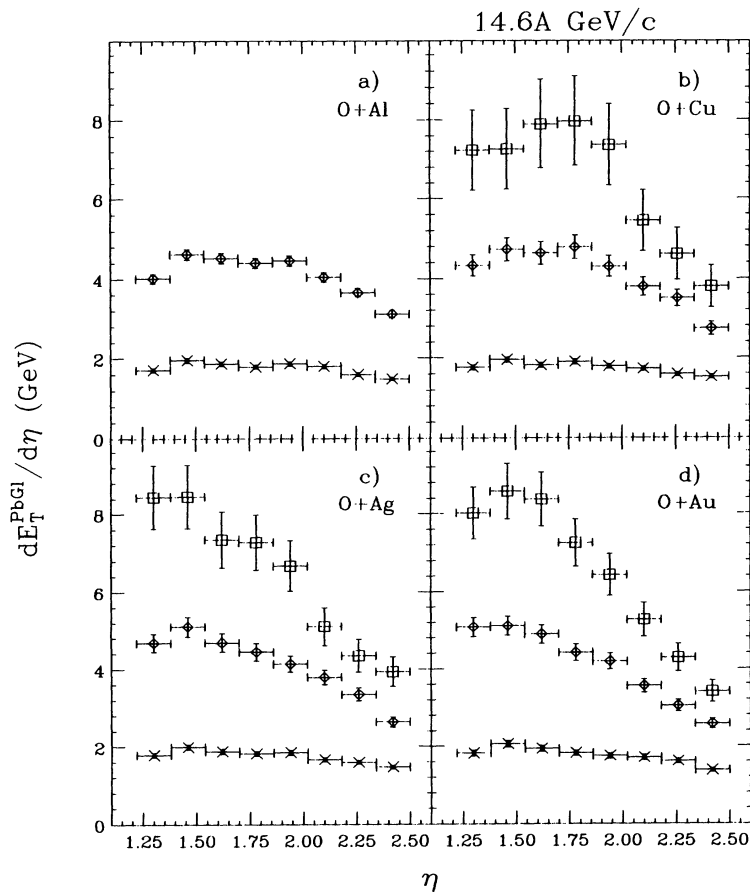
14.6A GeV/c

FIG. 9. $dE_T^{PbGl}/d\eta$ for O+A reactions. The diagonal cross-shaped points are for the slice $2.0 < E_T^{PbGl} < 2.5$ GeV; the diamond-shaped points are for the slice $5.0 < E_T^{PbGl} < 5.5$ GeV; the square points are for the slice $8.0 < E_T^{PbGl} < 8.5$ GeV. (a) O+Al, (b) O+Cu, (c) O+Ag, and (d) O+Au.

14.6A GeV/c
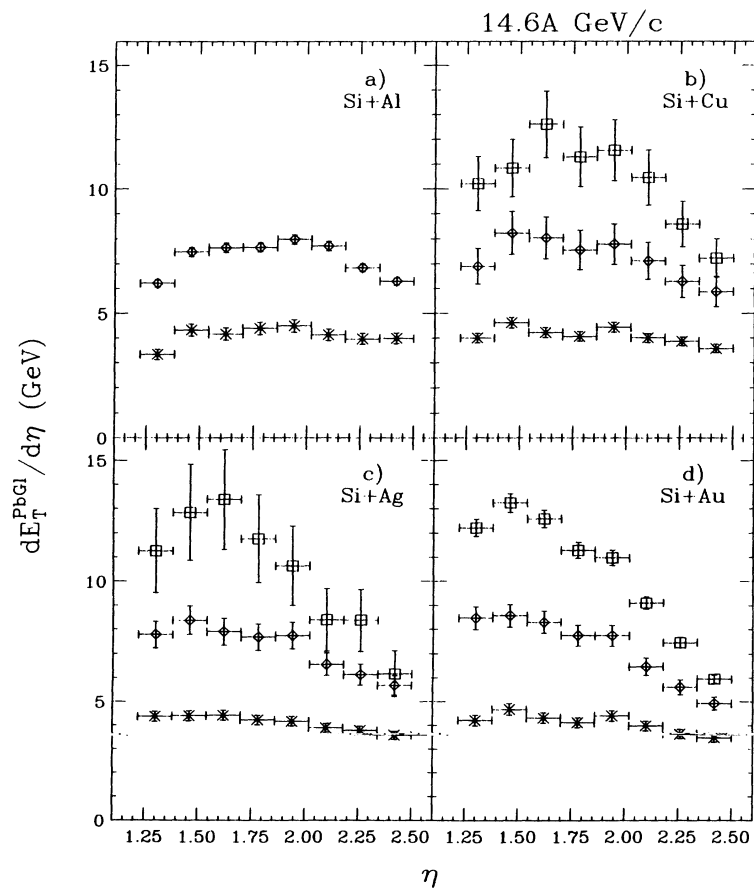

FIG. 10. $dE_T^{PbGl}/d\eta$ for Si+A reactions. The diagonal cross-shaped points are for the slice $5.0 < E_T^{PbGl} < 5.5$ GeV; the diamond-shaped points are for the slice $9.0 < E_T^{PbGl} < 9.5$ GeV; the square points are for the slice $13.0 < E_T^{PbGl} < 13.5$ GeV. (a) Si+Al, (b) Si+Cu, (c) Si+Ag, and (d) Si+Au.
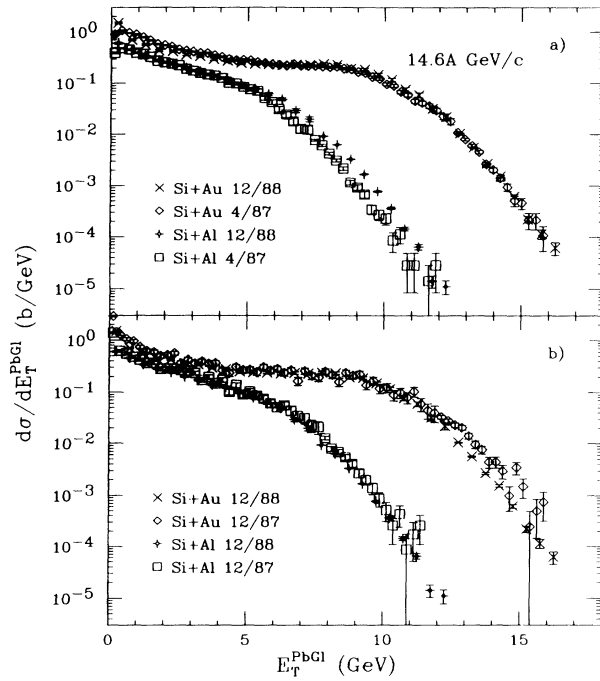
FIG. 11. Comparison of Si+Al and Si+Au $d\sigma/dE_T^{\mathrm{PbGl}}$ spectra (a) between the runs of December 1988 (these data) and April 1987 (Ref. [4], rescaled as explained in the text), and (b) between the runs of December 1988 and December 1987 (Ref. [19]).
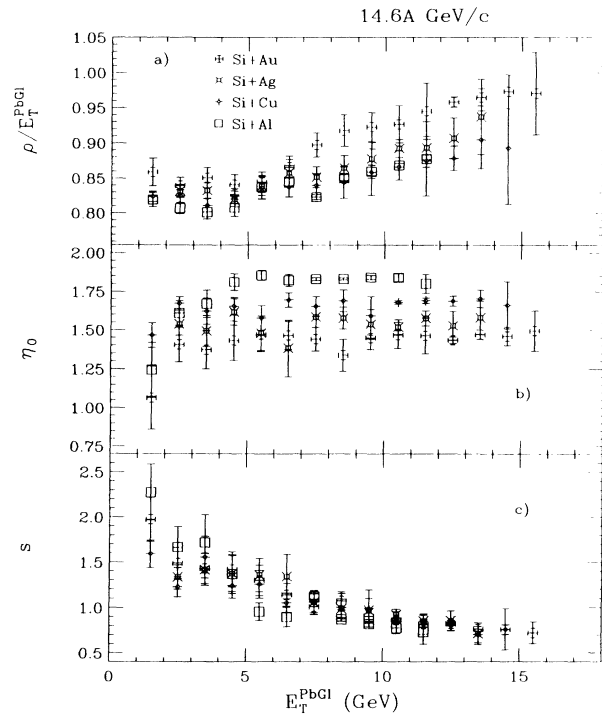

FIG. 12. Gaussian fit parameters for $dE_T^{\mathrm{PbGl}}/d\eta$ versus E_T^{PbGl} for Si+Au.

TABLE VI. Summary of Gaussian fits of the $dE_T^{\mathrm{PbGl}}/d\eta$ distributions to the form of Eq. (6).

E_T^{PbGl} (GeV)	ρ (GeV)	η_0	s	$\chi^2/$d.o.f.
		p+Au		
0.75–1.00	0.93 ± 0.08	1.15 ± 0.26	0.95 ± 0.17	1.01
1.00–1.25	1.09 ± 0.04	1.67 ± 0.04	0.58 ± 0.04	0.79
1.25–1.50	1.40 ± 0.08	1.68 ± 0.04	0.48 ± 0.04	2.69
1.50–1.75	1.83 ± 0.02	1.57 ± 0.01	0.47 ± 0.01	2.81
1.75–2.00	2.17 ± 0.03	1.61 ± 0.01	0.42 ± 0.01	8.04
2.00–2.25	2.59 ± 0.08	1.52 ± 0.03	0.44 ± 0.02	1.82
		O+Au		
1–2	1.33 ± 0.03	1.23 ± 0.11	1.41 ± 0.12	1.91
2–3	2.19 ± 0.03	1.41 ± 0.08	1.16 ± 0.10	0.70
3–4	3.18 ± 0.06	1.33 ± 0.09	1.12 ± 0.09	1.84
4–5	4.30 ± 0.09	1.33 ± 0.07	0.96 ± 0.06	0.16
5–6	5.41 ± 0.14	1.34 ± 0.08	0.87 ± 0.06	0.11
6–7	6.85 ± 0.44	1.21 ± 0.16	0.90 ± 0.11	0.34
7–8	7.63 ± 0.16	1.36 ± 0.05	0.79 ± 0.04	0.50
8–9	8.57 ± 0.33	1.44 ± 0.09	0.72 ± 0.07	0.20
		Si+Al		
1–2	1.23 ± 0.02	1.25 ± 0.17	2.28 ± 0.31	2.45
2–3	2.02 ± 0.02	1.61 ± 0.08	1.67 ± 0.23	4.10
3–4	2.80 ± 0.03	1.67 ± 0.09	1.72 ± 0.31	4.12
4–5	3.64 ± 0.06	1.81 ± 0.05	1.37 ± 0.21	2.30
5–6	4.61 ± 0.09	1.86 ± 0.03	0.95 ± 0.10	1.29
6–7	5.50 ± 0.15	1.82 ± 0.04	0.90 ± 0.11	0.67
7–8	6.17 ± 0.03	1.83 ± 0.01	1.12 ± 0.03	10.7

TABLE VI. (*Continued*).

Si+Al

E_T^{PbGl} (GeV)	ρ (GeV)	η_0	s	χ^2/d.o.f.
8–9	7.23 ± 0.04	1.83 ± 0.01	0.87 ± 0.02	8.82
9–10	8.17 ± 0.09	1.84 ± 0.01	0.82 ± 0.03	2.48
10–11	9.12 ± 0.22	1.84 ± 0.03	0.77 ± 0.06	0.62
11–12	10.1 ± 0.6	1.80 ± 0.06	0.73 ± 0.13	0.34

Si+Cu

E_T^{PbGl} (GeV)	ρ (GeV)	η_0	s	χ^2/d.o.f.
1–2	1.24 ± 0.01	1.47 ± 0.08	1.59 ± 0.15	5.49
2–3	2.06 ± 0.02	1.67 ± 0.04	1.22 ± 0.11	1.56
3–4	2.84 ± 0.03	1.62 ± 0.09	1.55 ± 0.23	1.68
4–5	3.71 ± 0.05	1.65 ± 0.06	1.24 ± 0.14	1.70
5–6	4.58 ± 0.07	1.58 ± 0.08	1.26 ± 0.15	1.39
6–7	5.44 ± 0.09	1.70 ± 0.05	1.05 ± 0.11	0.64
7–8	6.30 ± 0.13	1.65 ± 0.06	1.06 ± 0.13	1.36
8–9	7.17 ± 0.19	1.69 ± 0.07	1.00 ± 0.15	0.28
9–10	8.16 ± 0.31	1.59 ± 0.12	0.99 ± 0.20	0.44
10–11	9.10 ± 0.05	1.68 ± 0.01	0.86 ± 0.02	6.39
11–12	10.1 ± 0.1	1.69 ± 0.02	0.81 ± 0.03	2.98
12–13	11.0 ± 0.2	1.69 ± 0.03	0.80 ± 0.06	0.79
13–14	12.2 ± 0.6	1.70 ± 0.06	0.70 ± 0.09	0.08
14–15	13.0 ± 1.2	1.66 ± 0.15	0.76 ± 0.23	0.10

Si+Ag

E_T^{PbGl} (GeV)	ρ (GeV)	η_0	s	χ^2/d.o.f.
2–3	2.08 ± 0.02	1.54 ± 0.07	1.33 ± 0.13	2.07
3–4	2.91 ± 0.04	1.49 ± 0.10	1.42 ± 0.18	0.93
4–5	3.69 ± 0.05	1.62 ± 0.08	1.37 ± 0.20	0.69
5–6	4.62 ± 0.07	1.48 ± 0.11	1.36 ± 0.19	0.77
6–7	5.58 ± 0.12	1.38 ± 0.18	1.34 ± 0.24	1.02
7–8	6.39 ± 0.11	1.59 ± 0.07	1.06 ± 0.12	0.94
8–9	7.35 ± 0.15	1.58 ± 0.07	0.98 ± 0.11	0.70
9–10	8.34 ± 0.22	1.54 ± 0.10	0.97 ± 0.13	0.33
10–11	9.37 ± 0.13	1.52 ± 0.05	0.92 ± 0.06	1.10
11–12	10.3 ± 0.2	1.58 ± 0.05	0.85 ± 0.06	0.55
12–13	11.3 ± 0.4	1.53 ± 0.09	0.86 ± 0.11	0.23
13–14	12.7 ± 0.7	1.58 ± 0.11	0.71 ± 0.12	0.09

Si+Au

E_T^{PbGl} (GeV)	ρ (GeV)	η_0	s	χ^2/d.o.f.
1–2	1.29 ± 0.03	1.07 ± 0.20	1.97 ± 0.24	1.05
2–3	2.10 ± 0.03	1.41 ± 0.11	1.49 ± 0.17	2.42
3–4	2.98 ± 0.05	1.37 ± 0.12	1.43 ± 0.17	1.64
4–5	3.79 ± 0.06	1.43 ± 0.13	1.42 ± 0.20	1.31
5–6	4.65 ± 0.08	1.47 ± 0.11	1.30 ± 0.17	1.67
6–7	5.63 ± 0.10	1.47 ± 0.09	1.14 ± 0.12	0.98
7–8	6.73 ± 0.13	1.44 ± 0.08	1.01 ± 0.09	0.71
8–9	7.80 ± 0.19	1.34 ± 0.10	1.07 ± 0.10	1.18
9–10	8.77 ± 0.19	1.45 ± 0.07	0.90 ± 0.08	0.45
10–11	9.73 ± 0.28	1.47 ± 0.09	0.86 ± 0.09	0.47
11–12	10.9 ± 0.5	1.46 ± 0.12	0.82 ± 0.11	0.17
12–13	12.0 ± 0.1	1.43 ± 0.02	0.82 ± 0.02	3.67
13–14	13.0 ± 0.2	1.47 ± 0.03	0.76 ± 0.03	1.76
14–15	14.1 ± 0.4	1.46 ± 0.06	0.76 ± 0.05	0.39
15–16	15.0 ± 0.9	1.50 ± 0.13	0.72 ± 0.12	0.15

Si+Al,Cu,Ag,Au. The quantity plotted on the ordinate is

$$\frac{d\sigma}{d\rho} = \frac{d\sigma/dE_T^{PbGl}}{d\rho/dE_T^{PbGl}} = \frac{2\Delta}{\rho(E_T^{PbGl} + \Delta) - \rho(E_T^{PbGl} - \Delta)}\left[\frac{d\sigma}{dE_T^{PbGl}}\right]_{E_T^{PbGl}}, \tag{8}$$

where Δ is the width of the slice in E_T^{PbGl} used, namely, 0.5 GeV for the O+A spectra and 1.0 GeV for the Si+A spectra [22]. These acceptance-independent spectra retain the energy saturation effect of Fig. 8: the ratios of the cross sections in the tails of Si+Cu, Ag, and Au remain saturated at constant values which are little changed from the values shown in Fig. 8(b), although the errors in Fig. 13 are relatively large. Once again, it is emphasized that this observation is made only for the central rapidity region, and it is impossible from these data alone to know whether other effects are occurring outside the detector acceptance.

VI. PROJECTILE DEPENDENCE

A. Relative scaling of O+A and Si+A

An initial analysis of the projectile dependence is shown in Fig. 14(d), where it is observed that the $d\sigma/dE_T^{PbGl}$ spectrum for Si+Au roughly matches that for O+Au when the O+Au energy scale is shifted upwards
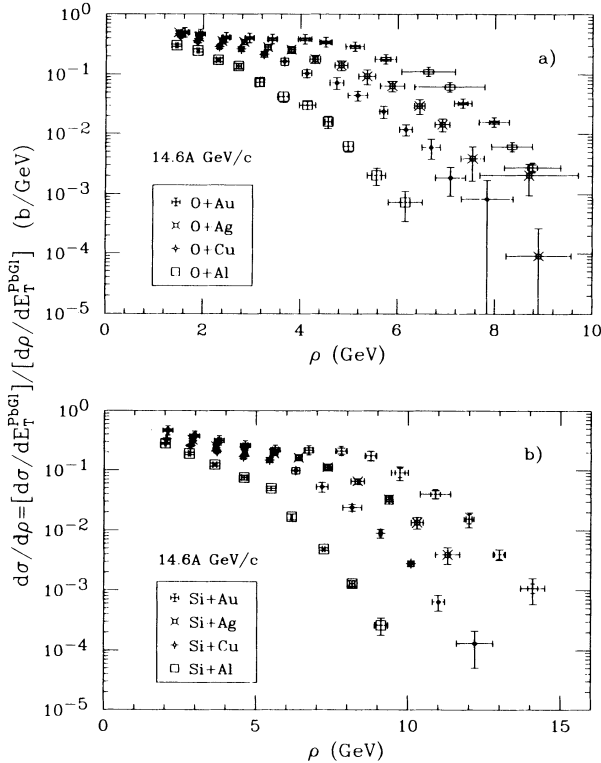
FIG. 13. The acceptance-independent differential cross section, $d\sigma/d\rho$, where $\rho = [dE_T^{PbGl}/d\eta]_{max}$. See Eq. (8) for the definition, and Sec. V of the text for further explanation. (a) O+Al,Cu,Ag,Au, and (b) Si+Al,Cu,Ag,Au.

by a factor of 1.64. Although not identical, the shapes of the two curves are very close, and one can rule out a scale change factor of $28/16 = 1.75$, as expected from simple projectile mass scaling. Indeed, if the O+Au energy scale is shifted upwards by 1.75, the plateau and knee of the curves match very well, but the tail of the O+Au scaled curve is well above the Si+Au data, indicating that the scaled slope is flatter [23]. Not ruled out is a scale change factor of 1.60, the ratio of the maximal total center-of-mass kinetic energy in the fireball model for the two reactions [24]. Another cautionary note is that the relative scaling analysis does not take into account possible effects due to the limited acceptance of the detector, such as the limited azimuthal acceptance (see Sec. VI B below.) Projectile scaling by the fireball model is seen in the NA35 data for O+Au and S+Au at 200 GeV/nucleon with a 2π azimuthal coverage [25].

Similarly, the O+Al spectrum is rescaled by a factor of 1.49 in Fig. 14(a), the O+Cu by 1.53 in Fig. 14(b), and the O+Ag by 1.61 in Fig. 14(c). All three lie very close to the corresponding Si+A curve. The fireball model predicts scale changes of 1.45, 1.56, and 1.59 for Al, Cu, and Ag, respectively. Simple rescaling of the transverse energy, however, cannot reproduce the target dependence of the spectra for a given projectile because the edges of the distributions are parallel (see Figs. 6 and 7).

B. Incoherent sum of $p + A$ compared with $A+A$

Since the earliest experiments with ultrarelativistic heavy ions, it has been known that the convolutions of proton-nucleus distributions may be used to describe the behavior of nucleus-nucleus spectra using a wounded projectile nucleon model (WPNM) [3, 26, 27]. In such a model, the number of struck, or "wounded," projectile nucleons is counted, but not the number of times each was struck. Unlike a "first collision" model, unwounded projectile nucleons are allowed to strike a previously wounded target nucleon and still be counted. The early experiments showed that the 16-fold convolution of the p+Au distribution matches very well the high-energy tail from ^{16}O+A, if the target, A, is copper or heavier at AGS energies [3], or if the target is lead at CERN energies [26, 27]. It is desirable to repeat this type of calculation with the present data because of the improved coverage (greater counting statistics) of the present set, especially for the $p + A$ spectra. (The p+Au measurements in Refs. [3] and [26] only covered about two decades in differential cross section.)

The geometry of the nucleus-nucleus collisions was modeled using a Monte Carlo calculation [28] which averaged over all impact parameters to obtain the distribution in the number of interacting projectile nucleons. A total inelastic nucleon-nucleon cross section of 30 mb,

corresponding to an absorption mean free path of 2.2 fm, was used in the calculation.

Another ingredient in this study was a fit to the form of Eq. (3) performed on the p+Au E_T^{PbGl} spectrum. From the summary in Table III, the total cross section for events in the detector is 1496 ± 25 mb. For the best agreement with the WPNM, the total p+Au inelastic cross section, $\sigma_{\mathrm{tot,inel}}$, is taken to be 1662 mb [29]. Thus, there is a small, but significant, probability,

$$p_0 = 1 - \frac{\sigma_{\mathrm{tot,det}}}{\sigma_{\mathrm{tot,inel}}} = 1 - \frac{1496 \text{ mb}}{1662 \text{ mb}} = 0.10, \qquad (9)$$

that a proton interacting with the Au target will not produce a signal in the lead-glass detector. (Recall that the detector only covers half of the possible azimuthal angles.) For the present case we write the probability distribution for one projectile nucleon to interact in the target and produce transverse energy, E_T, as

$$P_1(E_T) = (1 - p_0)f_1(E_T) + p_0\delta(E_T), \qquad (10)$$

where δ is the Dirac delta function, and f_1 is the probability distribution given that the detector has a nonzero signal. If the total probability distribution P_1 is convo-

luted with itself $n - 1$ times, the result is P_n, the total probability distribution for n independently interacting projectile nucleons. Convoluting Eq. (10), we find

$$P_n(E_T) = \sum_{i=0}^{n} \binom{n}{i} p_0^{n-i}(1 - p_0)^i f_i(E_T), \qquad (11)$$

where

$$\binom{n}{i} = \frac{n!}{(n-i)! \, i!} \qquad (12)$$

is the binomial coefficient, and f_i is the result of convoluting f_1 with itself $i - 1$ times. By definition, $f_0(E_T) = \delta(E_T)$.

Following Eq. (3), we set

$$f_1(E_T) = b\left[\frac{\varepsilon}{\Gamma(p_1)}(bE_T)^{p_1-1} + \frac{1-\varepsilon}{\Gamma(p_2)}(bE_T)^{p_2-1}\right]e^{-bE_T}. \qquad (13)$$

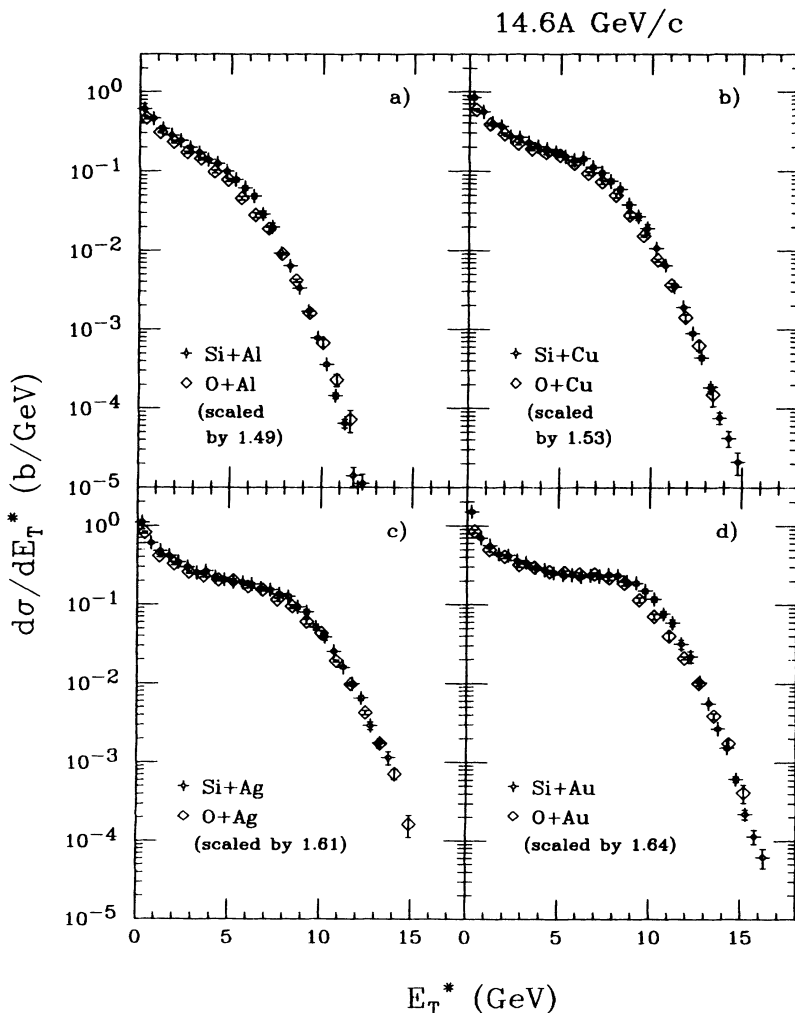A straightforward calculation of the convolutions of Eq. (13) shows that, for $i \geq 1$,

14.6A GeV/c

FIG. 14. Comparison between the $d\sigma/dE_T^{\mathrm{PbGl}}$ spectra of Si+A and O+A. The O+A spectra have E_T^{PbGl} rescaled while the Si+A have no such rescaling. (a) Si+Al compared to O+Al rescaled by the factor 1.49, (b) Si+Cu compared to O+Cu rescaled by the factor 1.53, (c) Si+Ag compared to O+Ag rescaled by the factor 1.61, and (d) Si+Au compared to O+Au rescaled by the factor 1.64.

$$f_i(E_T) = \sum_{j=0}^{i} \binom{i}{j} \varepsilon^j (1-\varepsilon)^{i-j} \frac{b}{\Gamma(p_{ij})} (bE_T)^{p_{ij}-1} e^{-bE_T},$$

$$(14)$$

where

$$p_{ij} = jp_1 + (i-j)p_2.$$

$$(15)$$

The WPNM prediction for the nucleus-nucleus spectrum is found by weighting each of the probability distributions, P_n, by the geometric probabilities from the Monte Carlo calculation. In other words,

$$\left(\frac{d\sigma}{dE_T}\right)_{\text{WPNM}} = \sigma \sum_{n=1}^{n_{\text{proj}}} w_n P_n(E_T),$$

$$(16)$$

where σ is the total nucleus-nucleus cross section observed experimentally and listed in Tables IV and V, n_{proj} is the total number of nucleons in the projectile, and w_n is the probability that the number of interacting projectile nucleons is n.

The WPNM results are shown and compared to the measured data in Figs. 15 and 16, for O+Al,Cu,Ag,Au

and Si+Al,Cu,Ag,Au, respectively. The top curve is the predicted $(d\sigma/dE_T^{\text{PbGl}})_{\text{WPNM}}$ as given by Eq. (16); the lower curves show the individual terms $\sigma w_n P_n(E_T^{\text{PbGl}})$, for $n = 1, \ldots, n_{\text{proj}}$. The p+Au spectral fit given in Table III provided the parameters b, ε, p_1, and p_2 for all projectiles and targets.

All of the predicted curves for $(d\sigma/dE_T^{\text{PbGl}})_{\text{WPNM}}$ agree very well with the data (points) in the peripheral, or "plateau" region. As reported earlier for different detector configurations [3, 26], the predicted high-energy edges ("tails") of O+Au and O+Cu also match the data very well. Finally, the Si+Au tail is actually underpredicted by an amount that corresponds to an energy scale shift of approximately 6–7 %.

It may be argued that the use of the p+Au spectrum as the basis for the convolution is naive, if not misleading, because of the lower mean value of E_T^{PbGl} of this distribution compared to distributions of p+Al and p+Cu, as described in Sec. III A. To address this issue, the convolution analysis was repeated using the p+Al spectrum (and the appropriate value $p_0 = 0.21$) as the basis for the convolution. The results were indistinguishable from those shown in Figs. 15 and 16. Since the p+Al and
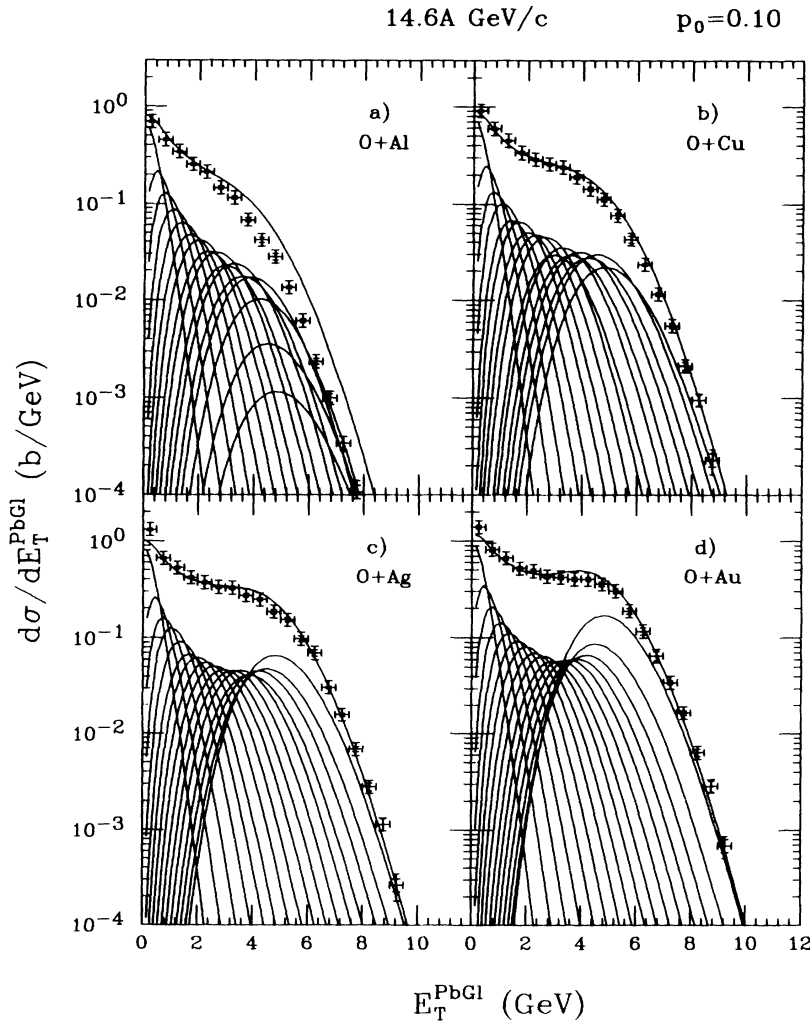
14.6A GeV/c   **p$_0$=0.10**

FIG. 15. Predicted O+A spectra from the wounded projectile nucleon model. The points are the measured data; see text for explanation of the curves. (a) O+Al, (b) O+Cu, (c) O+Ag, and (d) O+Au.

p+Au spectra show the same behavior at high transverse energy, this indicates that it is the shape of the tail of the $p + A$ distribution, rather than the mean value of E_T^{PbGl}, which dominates the tails of the convoluted O+A and Si+A distributions.

In conclusion, the convolutions work well (to within 7% in energy) in the context of the wounded projectile nucleon model for targets of Cu and heavier. Stated another way, the general features of particle production in nucleus-nucleus collisions at these energies roughly agree with those expected from an incoherent sum of separate proton-nucleus collisions.

C. Attempt to reconstruct $p + A$ from p+Be

Proton-beryllium reactions typically involve only one nucleon-nucleon interaction, and therefore are very similar to proton-proton collisions. After using the Monte Carlo calculation described in Sec. VI B, the p+Be E_T^{PbGl} spectrum was deconvoluted in the context of the wounded-nucleon model (WNM) [30] in which wounded projectile and target nucleons are treated equally. Struck nucleons are counted in the same manner in the WNM

as in the WPNM described in Sec. VI B; however, it is the total number of struck nucleons that is convoluted in the WNM, not the number of struck projectile nucleons. It is assumed that each wounded nucleon has the same spectrum for produced particles.

Deconvolution of the p+Be spectrum yielded a $p + p$ spectrum, which was then convoluted back to give the WNM predictions for the spectra of p+Al, p+Cu, and p+Au. The calculated spectra are shown in Fig. 17, along with the data for p+Be and p+Au. The convoluted curves are normalized by the total cross sections given in Table III. The failure of the WNM for this case is striking, demonstrating, for example, that the second wounded target nucleon in p+Au is not as efficient a source of produced particles at midrapidity as the first wounded target nucleon. Note that identical shapes for all $p + A$ spectra, independent of target, is an inherent assumption of the WPNM.

VII. CONCLUSIONS

The general picture of reactions at 14.6 GeV/c per nucleon that emerges from these data is one with a large
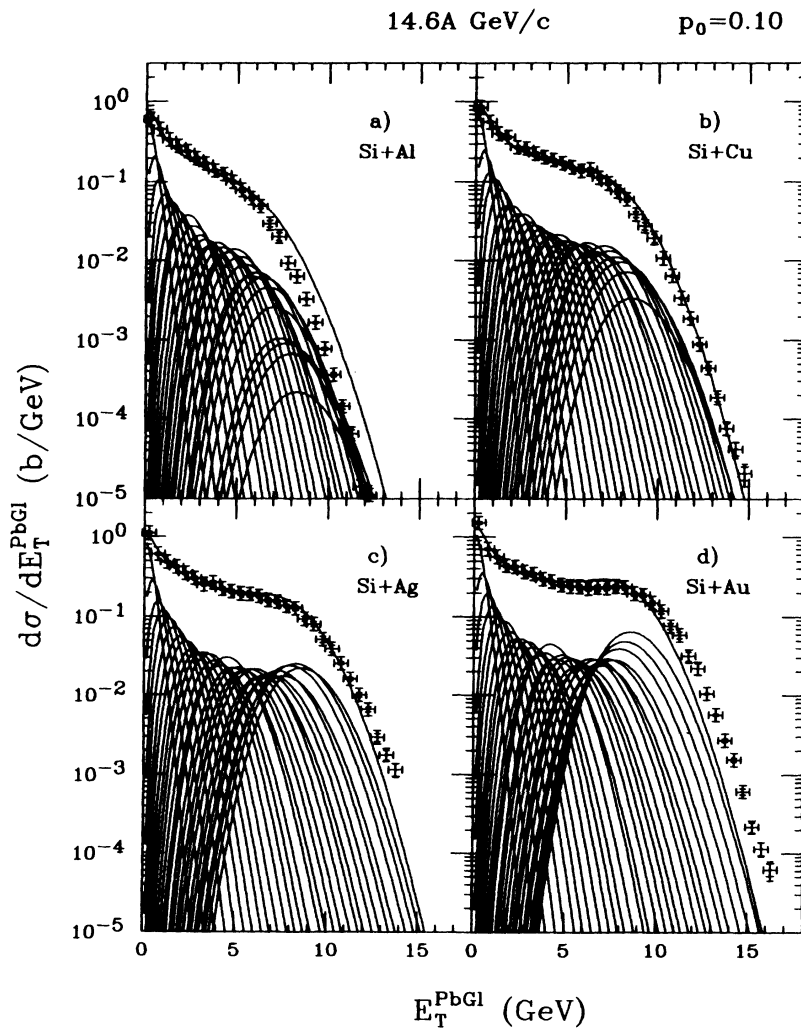

FIG. 16. Predicted Si+A spectra from the wounded projectile nucleon model. The points are the measured data; see text for explanation of the curves. (a) Si+Al, (b) Si+Cu, (c) Si+Ag, and (d) Si+Au.
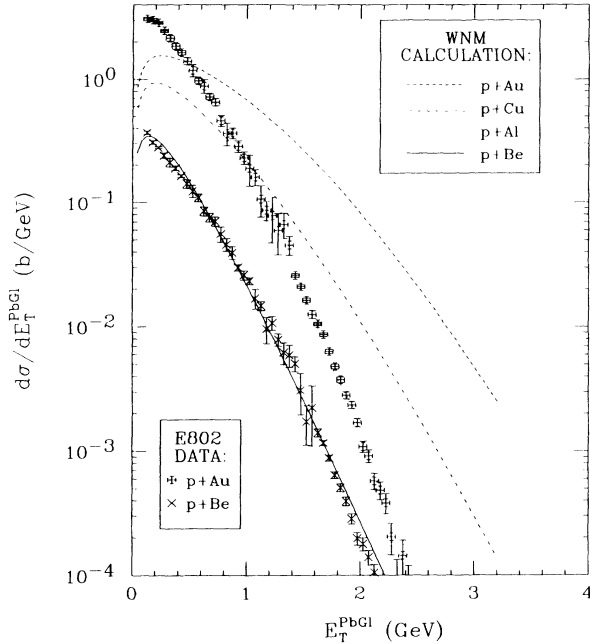
FIG. 17. Predicted $p + A$ spectra in the wounded-nucleon model, based on a deconvolution of the $p+$Be spectrum. The points are the measured data.

example, the Al target does not present a large enough cross section of fully central collisions for the transverse energy tail to reach its "saturated" value. For targets of Cu and heavier, however, the high-energy tails do indeed reach similar values. In comparing Ag and Au, the ratio of the $d\sigma/dE_T^{\text{PbGl}}$ values at high E_T^{PbGl} is simply the geometric ratio of areas, in spite of the difference in thickness of the two target nuclei.

To a remarkable degree, each of the Si+A $d\sigma/dE_T^{\text{PbGl}}$ spectra resembles the corresponding O+A spectrum with the energy rescaled by a factor that is close to the factor predicted by the fireball model.

While not perfect, the WPNM convolution calculations in Sec. VI B are generally successful at reproducing the energy scale of measured nucleus-nucleus spectra at the AGS incident energy. Therefore, for projectiles small compared to the target, spectra from nucleus-nucleus reactions are described by the incoherent sum of proton-nucleus spectra. Symmetric colliding systems test different geometries than the highly asymmetric, and large systems may be different from small. Hence there may be surprises ahead from future experiments with Au+Au.

In conclusion, global transverse energy spectra are a valuable probe of the complex reactions of relativisitic heavy ions. Together with complementary probes, such as inclusive particle spectra, a fuller understanding of particle production dynamics under the extreme conditions of these reactions emerges.

amount of projectile "stopping," in the sense of exhaustion of particle production. For the proton beam, all targets from Be to Au show the same spectral shape (except at the lowest values of E_T^{PbGl}). $p+$Be reactions look much like elementary nucleon-nucleon reactions since they involve an average of 1.4 nucleon-nucleon collisions. Hence particle production at midrapidity in $p+$Au must also be dominated by the first nucleon-nucleon collision, especially for events with high E_T. From the nucleus-nucleus lead-glass data gated by the forward calorimeter [31], it appears that second collisions also play a role.

For the nuclear projectiles ^{16}O and ^{28}Si, the geometry of the collision begins to play a more important role. For

ACKNOWLEDGMENTS

[1] J. D. Bjorken, Phys. Rev. D **27**, 140 (1983); L. McLerran, in *Proceedings of the Fourth International Conference on Ultra-Relativistic Nucleus-Nucleus Collisions, Quark Matter '84*, edited by K. Kajantie (Springer-Verlag, Berlin, 1985), p. 1.

[2] AFS Collaboration, H. Gordon *et al.*, Phys. Rev. D **28**, 2736 (1983); BCMOR Collaboration, A. L. S. Angelis *et al.*, Phys. Lett. **141B**, 140 (1984); **168B**, 158 (1986).

[3] E802 Collaboration, T. Abbott *et al.*, Phys Lett. B **197**, 285 (1987).

[4] E802 Collaboration, L. P. Remsberg *et al.*, Z. Phys. C **38**, 35 (1988).

[5] E814 Collaboration, P. Braun-Munzinger *et al.*, Z. Phys. C **38**, 45 (1988); J. Barrette *et al.*, Phys. Rev. Lett. **64**, 1219 (1990).

[6] NA34 Collaboration, T. Akesson *et al.*, Z. Phys. C **38**, 383 (1988); J. Schukraft *et al.*, Nucl. Phys. **A498**, 67c

(1989).

[7] NA35 Collaboration, W. Heck *et al.*, Z. Phys. C **38**, 19 (1988).

[8] NA35 Collaboration, J. Bachler *et al.*, University of Frankfurt Report No. IKF91-1 (1991).

[9] WA80 Collaboration, R. Albrecht *et al.*, Phys. Lett. B **199**, 297 (1987); G. Young, *et al.*, Nucl. Phys. **A498**, 53c (1989); R. Albrecht *et al.*, Phys. Rev. C **44**, 2736 (1991).

[10] See, for example, M. J. Tannenbaum, Int. J. Mod. Phys. **A4**, 3377 (1989), and references therein.

[11] J. S. Beale *et al.*, Nucl. Instrum. Methods **117**, 501 (1974).

[12] D. E. Alburger *et al.*, Nucl. Instrum. Methods **A254**, 88 (1987).

[13] Y. Akiba, Ph.D. thesis, University of Tokyo, 1989 (Report No. INS-IM-6).

[14] E802 Collaboration, T. Abbott et al., Phys. Rev. Lett. **64**, 847 (1990).

[15] M. J. Tannenbaum, in *Proceedings of the Workshop on Heavy Ion Physics at the AGS*, edited by O. Hansen, National Technical Information Service, 1990 (Report No. BNL-44911), p. 45.

[16] E802 Collaboration, T. Abbott et al., Phys. Rev. Lett. **66**, 1567 (1991).

[17] E802 Collaboration, T. Abbott et al., Nucl. Instrum. Methods **A290**, 41 (1990).

[18] Nucleus-nucleus measurements using 1% (Si) interaction length targets were also performed and gave target-out corrected spectra identical to those from the 3% targets.

[19] M. J. Tannenbaum, Nucl. Phys. **A488**, 555c (1988).

[20] H. von Gersdorff et al., Phys. Rev. C **39**, 1385 (1989).

[21] NA34 Collaboration, T. Akesson et al., Nucl. Phys. **B353**, 1 (1991).

[22] In the case of O+Au, where the errors on ρ are large for some points, the value of $d\rho/dE_T^{\text{PbGl}}$ came from a linear fit to ρ as a function of E_T^{PbGl}.

[23] This is true for all targets measured, and is expected in any convolution model, but not in a fireball model. See the later discussion.

[24] In a head-on O+Au collision, 16 projectile nucleons sweep out a core of 53 target nucleons; for Si+Au, 28 projectile nucleons sweep out 75 target nucleons. At an incident momentum of 14.6 GeV/c per nucleon, the total center-of-mass kinetic energy available in such a model is 96 GeV for O+Au, and 155 GeV for Si+Au.

[25] H. G. Ritter, Nucl. Phys. **A488**, 651c (1988).

[26] NA35 Collaboration, A. Bamberger et al., Phys. Lett. B **184**, 271 (1987).

[27] J. Ftacnik, K. Kajantie, N. Pisutova, and J. Pisut, Phys. Lett. B **188**, 279 (1987).

[28] H. Brody, S. Frankel, W. Frati, and I. Otterlund, Phys. Rev. D **28**, 2334 (1983).

[29] The value $\sigma_{\text{tot,inel}} = 1662$ mb derives from the interaction cross section of a wounded-nucleon Monte Carlo calculation. The experimental value for the total inelastic p+Au cross section at 20 GeV/c from S. P. Denisov et al., Nucl. Phys. **B61**, 62 (1973), is approximately 100 mb higher. Use of a different value of $\sigma_{\text{tot,inel}}$ will change the results of this section somewhat.

[30] A. Bialas, M. Bleszynski, and W. Czyz, Nucl. Phys. **B111**, 461 (1976).

[31] E802 Collaboration, T. Abbott et al., Phys. Rev. C **44**, 1611 (1991).
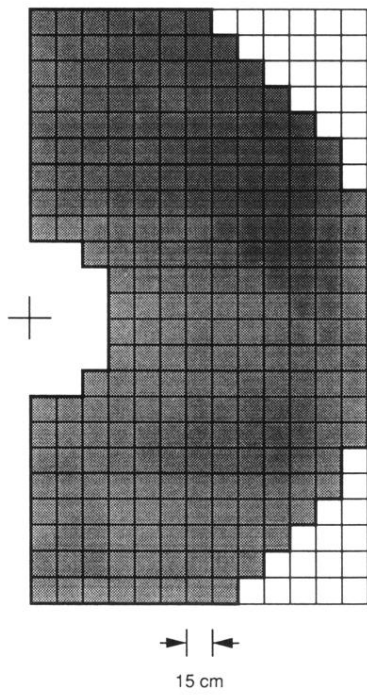
FIG. 1.   Arrangement of the 245 lead-glass blocks to form
an array covering half of the azimuthal angles. The cross hair
marks the position of the beam axis, which goes into the page.